

Cancer Therapeutic siRNA Delivery and Imaging by Nitrogen and
Neodymium-Doped Graphene Quantum Dots

by

Alina Valimukhametova

Bachelor of Science, 2017
Kazan Federal University
Kazan, Russian Federation

Master of Science, 2019
Kazan Federal University
Kazan, Russian Federation

Submitted to the Graduate Faculty of the
College of Science and Engineering
Texas Christian University
in partial fulfillment of the requirements
for the degree of

Master of Science

March 2023

Cancer Therapeutic siRNA Delivery and Imaging by Nitrogen
and Neodymium-Doped Graphene Quantum Dots

by

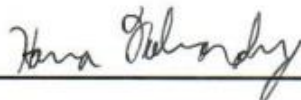
ALINA VALIMUKHAMETOVA

Dissertation Approved:



Major Professor









For The College of Science & Engineering

This page is intentionally left blank

ACKNOWLEDGEMENTS

I would like to express my deepest gratitude to my advisor Dr. Anton V. Naumov for his invaluable supervision, and unwavering support to accomplish this work. His continuous encouragement, patience, and excellent mentorship help me to overcome crucial steps related to research projects. I am grateful to my committee members Dr. Zygmunt (Karol) Gryczynski, Dr. Hana Dobrovolny, and Dr. Giridhar Akkaraju for their time, suggestions, and advice to successfully complete this research and write this thesis. I am also thankful to all other faculty members, staff, and my fellow graduate students of the Physics and Astronomy Department for offering assistance and advice when needed. Last but not the least, I am extremely thankful to my family and friends for their unending support and love.

Table of Contents

ACKNOWLEDGEMENTS	ii
LIST OF FIGURES	v
LIST OF ABBREVIATIONS	viii
1. Introduction	1
1.1. Motivation	1
1.2. Questions to be answered	2
1.3. Significance and innovation	2
1.3. Background Study	4
1.3.1. Cancer.....	4
1.3.2. Fluorescence.....	6
1.3.3. Western blot analysis.....	7
1.3.4. Graphene quantum dots	9
1.4. Overview	11
2. Experimental Methods and Equipment	19
2.1. Synthesis of NGQDs and Nd-NGQDs	19
2.2. Complexation of NGQDs and Nd-NGQDs with siRNAs	20
2.3. Structural Characterization.....	20
2.4. Optical Characterization.....	21
2.5. Electrokinetic Characterization	21
2.6. Cell studies	22
3. Results and discussion.....	25
Are graphene quantum dots suitable for siRNA delivery with imaging capabilities?.....	25
3.1. Size characterization.....	25
3.2. Optical properties	27
3.3. GQD/siRNA complex characterization	29
3.4. Cell Viability	33
Can GQD/siRNA complexes be used for imaging in vitro?	35
3.5. Internalization/excretion study of GQDs.....	35
3.6. Internalization of GQD/siRNA complexes.....	37
Does the GQD/siRNA complexes lead to cancer gene silencing?	40
3.7. Protein knockdown by GQD/siRNA complexes	40

4. Conclusion.....	43
4.1. Conclusion.....	43
4.2. Questions answered.....	44
4.3. Future Studies.....	45
References	48
VITA	
Abstract	

LIST OF FIGURES

Figure 1. Schematic illustration of principle of western blot technique [45].	8
Figure 2. Reaction of HRP with 4CN in the presence of H ₂ O ₂ .	8
Figure 3. Molecular visualization of NGQDs geometrically optimized with MMFF94 energy minimization calculation	9
Figure 4. Schematic illustration of RNAi mechanism. After entering cell siRNA binds to RNA-induced silencing complex (RISC) where the antisense chain is loaded onto the RISC, and the sense chain is discarded. Then mRNA is targeted by the antisense chain and undergoes cutting and degradation [91]	12
Figure 5. 808 nm excited Nd ³⁺ system, and the corresponding mechanisms for NIR emission [128].	18
Figure 6. The schematic of Nd-NGQDs synthesis.	19
Figure 7. TEM images and size distributions of (a) NGQD (4.0±0.6 nm) and (b) Nd-NGQDs (3.8±0.9 nm). HRTEM images of NGQDs (c) and Nd-NGQDs (d) with corresponding characteristic graphitic lattice spacings. Inset: FFT image. (e) EDX spectra of Nd-NGQDs. Inset: Weight/atomic percentages of Carbon, Nitrogen, Oxygen and Neodymium.	26
Figure 8. FTIR spectra of NGQDs and Nd-NGQDs. NGQDs spectrum is shifted up by 10 % for visualization.	27
Figure 9. (a) UV-VIS absorption spectra of NGQDs and Nd-NGQDs. (b) NIR absorption spectra of Nd-NGQDs at 10 mg/mL concentration.	28
Figure 10. (a) NIR fluorescence of Nd-NGQDs at the concentration of 11.3 mg/mL with 808 nm laser excitation. (b) Visible fluorescence of NGQDs (black) and Nd-NGQDs (red) at 10 and 11.3 mg/mL concentrations with 400 nm xenon lamp excitation.	29
Figure 11. Zeta potential of siKRAS, siEGFR, NGQDs, Nd-NGQDs and NGQD/siEGFR, NGQD/siKRAS, Nd-NGQD/siEGFR and Nd-NGQD/siKRAS complexes at 1:0.01 w/w ratio.	30

Figure 12. Gel retardation assay of (a) NGQD/siEGFR, (b) NGQD/siKRAS, (c) Nd-NGQD/siEGFR, (d) Nd-NGQD/siKRAS complexes at different w/w ratios.....	31
Figure 13. Molecular visualization of NGQD/siEGFR complex geometrically optimized with MMFF94 energy minimization calculation. Inset: zoomed-in area showing the proximity of NGQD amine siEGFR phosphate groups.	32
Figure 14. (a) HRTEM and (b) TEM images of NGQD/siEGFR complex at 1:0.01 weight ratio.....	33
Figure 15. Cell viability of HeLa cells after treatment with (a) NGQD/siEGFR and NGQD/siKRAS, (b) Nd-NGQD/siEGFR and Nd-NGQD/siKRAS complexes at 1:0.01 weigh ratio.....	34
Figure 16. (a) Cellular internalization/excretion dynamics of Nd-NGQDs samples over 1, 6, 12, 24, and 48 h based on the fluorescence intensity of Nd-NGQDs within the HEK-293 cells in the VIS (460 nm excitation, 540 nm emission). (b) Bright-field/VIS fluorescence confocal overlay images of HEK-293 cells treated with Nd-NGQDs at their optimal internalization time point of 12 hours.....	35
Figure 17. (a) Cellular internalization/excretion dynamics of Nd-NGQDs samples over 1, 6, 12, 24, and 48 h based on the fluorescence intensity of Nd-NGQDs within the HEK-293 cells in the NIR (808 nm excitation, 1060 nm emission). (b) Bright-field/NIR fluorescence overlay images of HEK-293 cells treated with Nd-NGQDs at their optimal internalization time point of 12 hours.....	37
Figure 18. Bright field/visible fluorescence confocal overlay images of HeLa cells treated with (a) NGQD/siEGFR-ROX, (b) NGQD/siKRAS-ROX, (c) NGQD/siEGFR-ROX and (d) Nd-NGQD/siKRAS-ROX for 12 h. GQD (shown in green) is excited with 480 ± 20 nm and collected at 535 ± 20 nm, ROX (shown in orange) is excited with 540 ± 20 nm and collected at 600 ± 20 nm. (c) and (d) also include the overlay of NIR fluorescence arising from internalized Nd-NGQDs. Nd-NGQD (shown in red) is excited with 808 nm laser and collected in the range of 850-1350 nm. (b) Inset: 3D confocal image of green GQD and orange ROX fluorescence in the HeLa cell treated with NGQD/siKRAS-ROX.	38
Figure 19. Western blots of NGQDs and Nd-NGQDs at 375 $\mu\text{g/mL}$ concentrations.	40

Figure 20. Representative Western blot images and quantification of the blots upon the treatment of HeLa cells with (a) NGQD/siEGFR and Nd-NGQD/siEGFR, (b) NGQD/siKRAS and Nd-NGQD/siKRAS complexes at different GQD/siRNA weight ratios. Lipofectamine 3000 is used as a positive control. EGFR and KRAS protein expression is normalized by actin protein loading and presented as percentage of the untreated sample. Values represent the mean \pm SE of three independent experiments. 42

LIST OF ABBREVIATIONS

GQDs: Graphene quantum dots

NGQDs: Nitrogen-doped graphene quantum dots

Nd-NGQDs: Neodymium and nitrogen-doped graphene quantum dots

RNA: Ribonucleic acid

DNA: Deoxyribonucleic acid

siRNA: Small interfering ribonucleic acid

KRAS: Kirsten rat sarcoma virus

EGFR: Epidermal growth factor receptor

siKRAS: siRNA targeting KRAS

siEGFR: siRNA targeting EGFR

UV: Ultraviolet

VIS: Visible

NIR: Near-infrared

TKI: Tyrosine kinase inhibitor

RNAi: Ribonucleic acid interference

FDA: Food and Drug Administration

PEI: Polyethylenimine

SWCNTs: Single walled carbon nanotubes

GO: Graphene oxide

mRNA: Messenger ribonucleic acid

DI: Deionized

DEPC: Diethyl Pyrocarbonate

LIST OF ABBREVIATIONS

TEM: Transmission electron microscopy

HRTEM: High-resolution transmission electron microscopy

EDS: Energy Dispersive X-ray analysis

FTIR: Fourier transform infrared

DSU: Disk spinning unit

ROX: 5-(and 6)-Carboxy-X-rhodamine

TBE: Tris-Borate-Ethylenediaminetetraacetic acid

MTT: 3-(4,5-dimethylthiazol-2-yl)-2,5-diphenyltetrazolium bromide

PBS: Phosphate-buffered saline

RIPA: Radioimmunoprecipitation Assay

BSA: Bovine serum albumin

SDS: Sodium dodecyl sulfate

TBS-T: Tris-buffered saline with 0.1% Tween® 20 detergent

MMFF94: Merck Molecular Force Field 94

QY: Quantum Yield

1. Introduction

1.1. Motivation

In the past decade, graphene quantum dots (GQDs), have emerged as a promising carrier for gene delivery with imaging capabilities in cancer therapeutics [1, 2]. GQDs are zero-dimensional nanostructures, consisting of few layers of graphene sheets with lateral dimensions generally below 20 nm. Due to the presence of a carbon lattice and, often, oxygen functional groups, GQDs have the capability to bind a variety of molecules through π - π stacking or electrostatic interactions. GQDs exhibit minimal toxicity *in vitro* and *in vivo* due to their smaller size and rapid excretion [3]. These properties render GQDs ideal candidates for the delivery of different therapeutic platforms. In addition to being a delivery agent, GQDs can also be utilized for imaging and biosensing. They are photostable and exhibit intrinsic fluorescence in the visible (VIS) and near-infrared (NIR), which can serve as a non-invasive detection and tracking mechanism [4, 5]. Several GQD-based optical sensors have recently been developed for the detection of RNA [6], ssDNA [7], miRNA [8], proteins [9], and small molecules [10, 11]. These advantageous properties of GQDs have not been fully utilized to date for small interfering RNA (siRNA) delivery, specifically those targeting Epidermal growth factor receptor (EGFR) and Kirsten rat sarcoma virus (KRAS), that can perform well against a variety of cancer types. This study aims to fill this gap by exploring the properties of GQDs, doped with nitrogen and neodymium, as standalone multifunctional agents for siRNA delivery with imaging capabilities in VIS/NIR spectral regions.

1.2. Questions to be answered

- i. Are GQDs suitable for siRNA delivery with imaging capabilities?

Here, we will study the properties of nitrogen- and neodymium-doped GQDs via structural and morphological characterization. We also employ absorption, fluorescence, and zeta-potential measurements. We will determine if GQDs can load siRNA non-covalently and perform a cell viability assay of GQD/siRNA complexes. This will indicate if the GQDs can be potentially utilized as a delivery agent with imaging capabilities and will be covered in chapters 3.1-3.4.

- ii. Can GQD/siRNA complexes be used for imaging *in vitro*?

This question requires us to determine the optimal time in which Nd-NGQDs are internalized in cells. We will also evaluate the ability of the GQD/siRNA complex to be internalized and imaged in HeLa cells. This will be done by using visible and near-infrared fluorescence properties of Nd-NGQDs, as well as siRNA tagged with carboxy-X-rhodamine (ROX) dye. This analysis will be discussed in chapters 3.5-3.6.

- iii. Does the GQD/siRNA complexes lead to cancer gene silencing?

At this point of the study, we will be looking to see if the GQD/siRNA complex lead to gene silencing and protein knockdown in HeLa cells. This step will be accomplished through western blot assay. We will determine if the GQDs can be used as a siRNA delivery vehicle in chapter 3.7.

1.3. Significance and innovation

The significance of this work is in the ability to address the critical needs of treating cancer caused by oncogenes and facilitate a safer and more effective genetic approach to cancer

therapeutics. The innovation of this work is two-fold. It involves *new approaches*: we utilize a novel gene silencing therapy that specifically suppresses oncogene expression in cancer cells, and *new materials* with imaging capabilities that efficiently deliver treatment and track it *in vitro*. The aforementioned experimental goals will be accomplished by developing nitrogen- and neodymium-doped graphene quantum dots that have: (1) capabilities for gene loading, (2) high biocompatibility, (3) photostability, (4) fluorescence in the visible (at 530 nm) with 460 nm excitation and (5) fluorescence in the NIR (at 1060 nm) with NIR excitation (808 nm).

1.3. Background Study

1.3.1. Cancer

Cancer is a disease characterized by uncontrolled cell growth. These cells may form tumors that can be cancerous [12]. Cancerous malignant tumors can spread to the different parts of the body via metastases and invade a variety of tissues to form new tumors. Cancer is a genetic disease that arises as a consequence of pathological changes in DNA due to (1) errors that occur as cells divide [13], (2) mutations due to carcinogens, such as tobacco [14], ultraviolet rays from the sun [15], and viruses, for example, human papillomavirus [16], or (3) inherited mutation errors in genes. Cancer cells, unlike normal cells, do not have a dependence on signals from other cells, responsible for their growth and division. They proliferate abnormally and survive high levels of stress compared to normal cells that would destroy themselves by apoptosis [17]. Generally, there are two main classes of mutant genes: oncogenes and tumor suppressor genes [12]. Oncogene has a dominant effect and makes the encoded protein hyperactive resulting in increased proliferation of cancerous cells. The tumor suppressor gene has an opposite origin, it inactivates the healthy cell activity. Both mutations are dangerous and lead to excessive cell survival and/or proliferation. While epigenetic changes do not affect the DNA of cells, they alter gene expression by changing how a cell reads a DNA sequence. Overall, understanding the alteration in cell behavior helps scientists to develop treatments for different types of cancer diseases.

In the past, there were only a few options for cancer treatment including surgery, radiation therapy, and chemotherapy [18, 19]. It was shown that surgery is most efficient only at an early stage of cancer, radiation damages both cancerous and non-cancerous cells, chemotherapy displays diminishing effectiveness as drug resistance develops, and does not

work for all types of cancer [20]. Thus, such conventional cancer therapies are limited by their inconvenience for patients, lack of specificity, and harmful side effects. Recently, a big emphasis has been put on novel modalities and approaches combined with conventional treatments [21-23]. Novel cancer treatments have been developed and are still under development, however, gene therapy points to the direction of future clinical products [24]. Gene therapy techniques involve the transfer of genetic material into cells in an effort to reverse an abnormal condition and treat cancer. This technique acts by replacing a mutated gene with a therapeutic gene, deactivating problem genes, causing gene knockdown, and introducing a new gene [24]. Gene therapy techniques include cancer vaccines [25], targeted therapy, for example, immunotherapy [26, 27], RNA interference (RNAi) [28], and CRISPR-Cas9 technologies [29].

Naked genetic materials are usually difficult to deliver due to rapid clearance and degradation by enzymes [30]. Numerous gene delivery systems and gene vectors have been developed for making the gene transfer efficient, safe, and specific to the target cells [31]. These delivery systems include viral vectors (retrovirus, adenovirus, lentivirus), and non-viral vectors (nanoparticles) [32-34]. Nanoparticles have been proven to be the most promising platforms for delivering genetic material [35] due to their size, selective gene delivery and targeting, and imaging modalities [36]. Unlike viral vectors, nanoparticles are beneficial in reducing the toxicities of treatment through selectivity, and reducing adverse effects [37]. Several types of nanoparticles are available as gene nanocarriers, including liposomes, micelles, metal nanoparticles, quantum dots and nanorods, and graphene quantum dots [38-40]. Graphene quantum dots (GQDs) recently have attracted growing attention from many researchers [1, 2]. They are more biocompatible, compared to quantum dots and nanorods,

chemically stable, and exhibit fluorescence in visible and near-infrared spectral regions, unlike organic nanoparticles.

1.3.2. Fluorescence

Fluorescence is an optoelectronic process in which a substance radiates light for a finite duration subsequent to the absorption of the excitation photon [41]. In order for that to happen, an electron in this substance located in the lower (ground) state is excited by an absorbed photon to the higher (excited) state. There it can undergo internal conversion, which is a non-radiative transition between two electronic states of the same multiplicity, and then falls to the lowest excited state. Being at the lowest excited state the electron can be returned to the ground state through a radiative transition, accompanied by the emission of a photon.

Fluorescence is usually characterized by excitation/emission wavelengths, its lifetime and quantum yield. Excitation and emission wavelengths determine the energies of the absorbed and emitted photon (second being greater than the first). The average time an electron spends in the excited state is called the lifetime and can be derived from the following equation:

$I(t) = I_0 e^{-\frac{t}{\tau}}$ where t is time, τ is the excited state lifetime, I_0 is fluorescence intensity at $t = 0$

s. Quantum yield (QY) determines the probability of a photon emission in the electronic transition. Quantum yield can be assessed with optical methods either absolutely with an integrating sphere gathering all emitted photons, or relatively to a fluorescence standard of known fluorescence quantum yield [42] with similar excitation and emission wavelengths. The

first method can be characterized by the following equation: $QY(\%) = \frac{S_2}{S_0 - S_1} \times 100$, where S_0

is a spectral area from incident light, S_2 is a spectral area emitted from sample, S_1 is a spectral area scattered from sample. The relative method of determining quantum yield is characterized

by the following equation: $\Phi_S = \Phi_R \left(\frac{I_S}{I_R}\right) \left(\frac{1-10^{-A_R}}{1-10^{-A_S}}\right) \left(\frac{n_S}{n_R}\right)^2$, where S and R denote the sample and reference, respectively, Φ_R is the known quantum yield of the reference standard, I is the integrated fluorescence spectrum intensity, A is the absorbance of the solution at the excitation wavelength (λ_{ex}), and n is the refractive index of the solution solvent. A single molecule may absorb and emit light multiple times, however, the excited-state energy is significantly higher than ground state energy, which increases the chances of the molecule undergoing irreversible photochemical degradation, called photobleaching. This is because fluorophores that are in the excited state are more likely to react with other molecules. The photobleaching of organic fluorophores are commonly explained by oxygen-dependent and oxygen-independent pathways [43]. Both mechanisms involve electronic excitations to triplet states since triplet states have longer lifetimes and are more reactive [44]. Molecular fluorophores commonly used in biological research, including DAPI, GFP, and indocyanine green, can only emit light for a couple of seconds before they photobleach, although the exact timescale depends on the excitation light intensity and molecular structure [43]. Utilizing photostable biomarkers not prone to photobleaching can aid in longer acquisition bioimaging improving both signal and elevating it over biological autofluorescence that also experiences photobleaching.

1.3.3. Western blot analysis

In order to validate the efficiency of oncogene-targeted cancer therapy it is crucial to evaluate its ability to initiate protein knockdown. For this purpose, the western blot technique is usually employed (Figure 1) [45]. Western blot is a reliable tool to analyze protein samples extracted from cells. Extracted proteins undergo gel electrophoresis and are transferred onto a nitrocellulose membrane that has a high affinity for protein. Transferred proteins are probed

with a primary antibody, then an enzyme-conjugated secondary antibody is attached to the primary one. As an enzyme, horseradish peroxidase (HRP) is commonly used for signal generation. Finally, the membrane with primary and secondary antibodies is incubated with the appropriate enzyme substrate (for example, 4-Chloro-1-naphthol (4CN)) to produce a signal (Figure 2). Here, the oxidation of 4CN is catalyzed by HRP leading to the formation of insoluble benzo-4-chlorocyclohexadienone. Since HRP is connected with the secondary antibody and protein of interest, respectively, the location and amount of the reaction product are correlated with the location and amount of the protein. As a result, the insoluble purple product is visible to the naked eye and can be detected with a CCD camera.

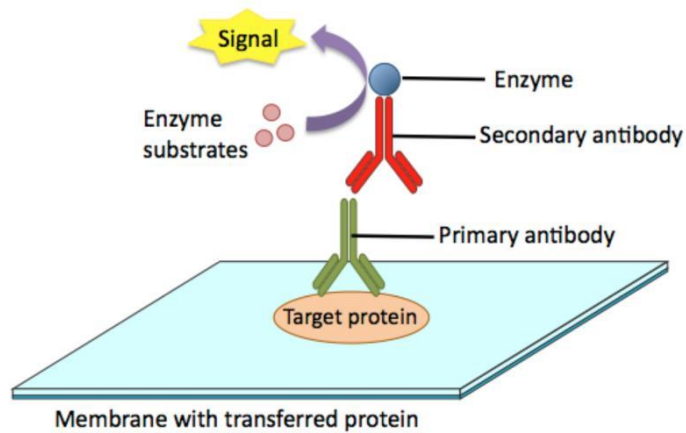


Figure 1. Schematic illustration of principle of western blot technique [45].

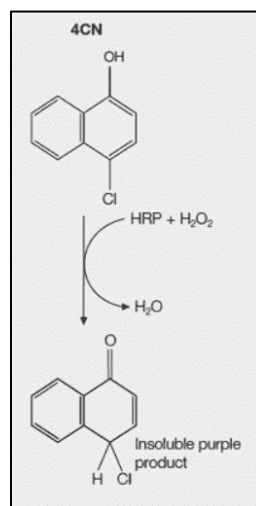


Figure 2. Reaction of HRP with 4CN in the presence of H_2O_2 .

1.3.4. Graphene quantum dots

Graphene quantum dots (GQDs) are small fragments of functionalized graphene with lateral dimensions generally below 20 nm (Figure 3). They are zero-dimensional (0D) structures and a result of the confinement of one-dimensional (1D) graphene nanoribbons [46]. GQDs exhibit unique optoelectronic properties that result in their applications ranging from optoelectronic devices to biomedical probes [2, 5, 47].

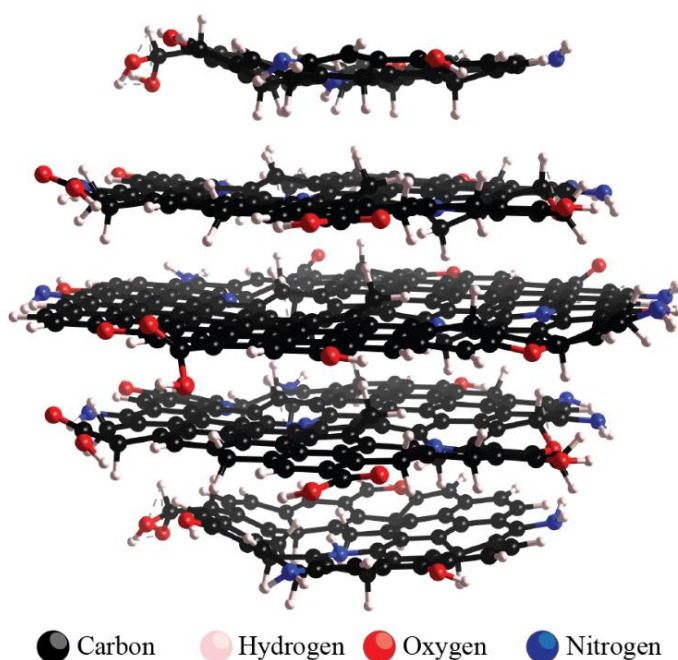


Figure 3. Molecular visualization of NGQDs geometrically optimized with MMFF94 energy minimization calculation

There are two routes to GQD synthesis, “top-down”, which is based on the decomposition of larger graphene-based materials into nanometer-scale GQDs, for example, arc-discharge method [46], laser ablation [48], chemical exfoliation and combustion [49, 50]; and “bottom-up”, such as microwave synthesis [51, 52], hydrothermal synthesis [53, 54], and thermal pyrolysis [55], involving further carbonization of small carbon-containing molecules used as precursor materials [56]. Due to the presence of a carbon lattice and, often, oxygen

functional groups, GQDs are soluble in water and have the capability to bind a variety of molecules through π - π stacking or electrostatic interactions. Oxygen addends also allow for covalent functionalization [1]. These properties render GQDs ideal candidates for the delivery of different therapeutic platforms. Compared to its relatives, single-walled carbon nanotubes (SWCNTs) and graphene oxide (GO), GQDs exhibit minimal toxicity *in vitro* and *in vivo* due to their smaller size and rapid excretion [3]. They can successfully deliver several drug and gene payloads [57-59]. For instance, the non-covalent transport of doxorubicin by the GQDs leads to improved chemotherapeutic efficiency with 10-fold lower treatment doses needed to produce the therapeutic effect in HeLa and MCF-7 cells [57]. GQDs, conjugated with plasmid DNA and MPG-2H1 chimeric peptide non-covalently facilitate their transfection into HEK-293 cells enabling gene delivery with nuclear targeting [59].

GQDs have a structure containing sp^2 domains and sp^3 hybridized carbon atoms (Figure 3), and therefore the origin of GQD fluorescence is still debatable. It has been attributed to the quantum-confinement effect, defect states, and functional groups [60, 61]. In GQDs functional groups disrupt the extended sp^2 hybridized carbons and isolate the sp^2 domains, thereby confining π electrons [62, 63]. This phenomenon gives rise to a finite band gap, and therefore fluorescence, generally in the visible spectral region [64]. Moreover, the visible fluorescence of GQDs is excitation wavelength dependent: different sizes of sp^2 graphitic regions can be excited and emit in resonance at different wavelengths. GQDs also demonstrate changes in fluorescence depending on the pH of the biological environment of cancerous and non-cancerous cell lines. Passivated functional groups on the surface of the GQDs affect GQD emission due to their protonation/deprotonation [65] and therefore render these nanoparticles capable of pH sensing.

The typical fluorescence lifetime range of graphene quantum dots is 2-5 ns, which is preferable for some optoelectronic and biological applications, including sensing, bioimaging, imaging of fingerprints in forensic science [66-69]. In addition, GQDs are resistant to photobleaching, unlike common dyes, due to their large aromatic and partially inorganic platform [70]. Several GQD-based optical sensors have recently been developed for the detection of RNA [6], ssDNA [71], miRNA [8], proteins [9], and small molecules [10, 11].

The successful siRNA delivery capability is recently shown by the GQDs synthesized bottom-up from glucose and tetraethylene pentaamine. When loaded with green fluorescent protein (GFP)-silencing siRNA, these GQDs form a stable complex, inhibiting GFP protein expression in HeLa cells [72]. Loaded with both aptamer and siRNA, GQDs can improve the efficiency of siRNA internalization into hepatocellular carcinoma cells inhibiting the expression of Fragile X mental retardation protein [73]. Similarly to other nanoparticles, when conjugated with polyethylenimine (PEI), GQDs exhibit enhanced siRNA loading via the electrostatic interaction of the negatively-charged gene with the cationic polymer [74-76]. Facile synthesis, the versatility of design and functionalization as well as useful optical properties and stability can allow GQDs to address the critical needs in gene delivery and *in vitro* imaging.

1.4. Overview

Cancer is a life-threatening disease that affects over one million people yearly in the United States alone [77, 78]. Pathological conditions associated with cancer result from the accumulation of multiple mutation-associated genetic and epigenetic changes [79]. In particular, oncogenes lead to the dysregulation of a variety of proteins in different forms of

cancer [80]. For instance, epidermal growth factor receptor (EGFR) and Kirsten rat sarcoma virus (KRAS) genes are frequently mutated in non-small lung cancer [81, 82]. Targeting EGFR and KRAS might provide an approach to lung cancer treatment as they play a crucial role in carcinogenesis causing the sustained proliferation of cells [83, 84]. Although EGFR responds well to tyrosine kinase inhibitor (TKI) therapy, drug resistance still remains a major issue [85]. According to recent studies, EGFR resistance to TKI therapy can be caused mainly by KRAS mutations, as KRAS is a downstream effector in EGFR signaling [86]. At the same time, KRAS is resistant to most available therapeutics and is difficult to target, making both EGFR and KRAS desired critical targets for cancer gene therapy [82, 87].

For the past decade, RNA interference (RNAi)-based therapeutics have attracted substantial attention in cancer therapy [88]. One of the major types of RNAi technology includes the delivery of small interfering RNA (siRNA), non-coding double-stranded oligos roughly 20-24 nucleotides in length. Unlike tyrosine kinase inhibitors that can act on multiple targets and might lack specificity [89], siRNA binds to a specific complementary mRNA sequence inducing its cleavage (Figure 4) [90].

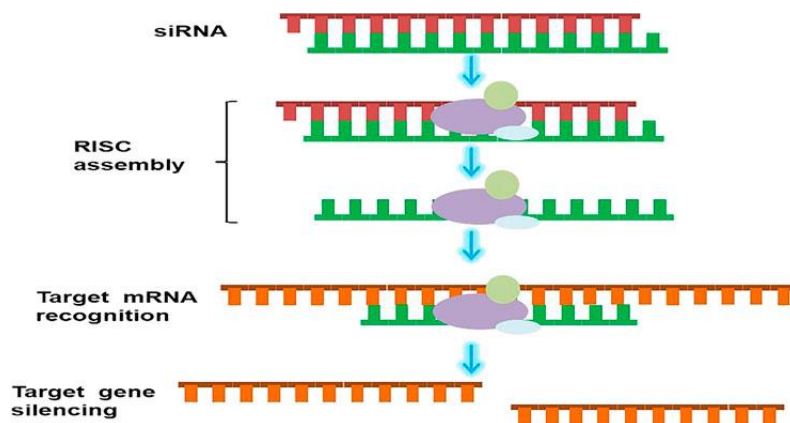


Figure 4. Schematic illustration of RNAi mechanism. After entering cell siRNA binds to RNA-induced silencing complex (RISC) where the antisense chain is loaded onto the RISC, and the sense chain is discarded. Then mRNA is targeted by the antisense chain and undergoes cutting and degradation [91]

In short, after entering the cell, double-stranded siRNA is loaded onto the RNA-induced silencing complex (RISC). The RISC discards one strand of the siRNA duplex and uses another strand to search and destroy complementary mRNA strand. This is a key step in the development of most RNAi therapies. Further, degradation of mRNA blocks the expression of the proteins, leading to its decrease and eventual knockdown. Thus, the knockdown of EGFR and KRAS proteins in cancer cells by RNAi technology will regulate their expression and stop carcinogenesis.

To date, the FDA has already approved four siRNA-based treatments making RNAi technology a prospective tool in gene silencing [92]. However, as a therapeutic method, RNAi technology is hampered by the inability of siRNA to transfect cells on its own, as well as its rapid enzymatic degradation in bodily fluids and tissues [93]. In order to overcome these obstacles, both viral and non-viral delivery vehicles have been developed [94]. While being highly effective, viral delivery vehicles can provoke a strong immune response, whereas their non-viral counterparts are considered more safe and versatile [95, 96]. For example, several types of lipid-based nanoparticles have been already FDA-approved for drug delivery [97] and demonstrate high transfection efficacy. In order to enable gene therapy to its fullest extent, modern nanocarriers have to protect the siRNA from serum nucleases, target the disease site to ensure high therapeutic accumulation and effective release, overcome biological barriers hampering gene transfection, facilitate endosomal escape, and possess delivery-tracking capabilities [98]. In this capacity solid nanoparticles are often more beneficial than their organic counterparts such as liposomes due to higher physical stability, versatile surface chemistry, tunable optical properties, and their potential for multimodality in delivery, targeting and image-based detection [99, 100].

Among solid nanoparticles, gold nanostructures have been used for siRNA transport due to their high biocompatibility, monodispersity, and ability for surface modification [101]. In several recent works gold nanoparticles conjugated with polyethylenimine (PEI) enable high gene transfection efficiency [102, 103]. PEI contains amine functional groups that are known to increase electrostatic interaction with siRNA and facilitate its internalization through the cell membrane as well as the endosomal escape. However, on its own PEI exhibits significant cellular toxicity [104] hampering the use of PEI-decorated nanoparticles in the clinic. Thus, the non-toxic incorporation of nitrogen groups within the nanomaterial is a highly desired option.

Carbon-based nanomaterials, such as single-walled carbon nanotubes (SWCNTs), can also serve as carriers for gene delivery [105, 106]. Due to their physical properties SWCNTs are able to enter cells, while their large aromatic platform allows for non-covalent therapeutic loading. Additionally, SWCNTs exhibit intrinsic fluorescence in the near-infrared (NIR) spectral region providing drug/gene delivery tracking capabilities [107]. Low biological autofluorescence, tissue absorption, and scattering in the NIR enhance the applicability of such image tracing to *in vivo* models [108]. SWCNTs can carry siKRAS and siEGFR, and facilitate an efficient knockdown of both target proteins *in vitro* and *in vivo* [109]. This leads to substantial cancer tumor growth rate inhibition, while the intrinsic SWCNT NIR fluorescence verifies the delivery of SWCNT/siRNAs complexes in biological cells and tumor tissues. SWCNT-based platforms are also explored for siRNA delivery in intact plant cells [110]. With topical administration involving some minor leaf puncture SWCNTs non-covalently formulated to mGFP5-silencing siRNA facilitate successful knockdown of this reporter gene. This indicates that SWCNT-assisted gene delivery is not limited to mammalian targets.

Another carbon-based nanomaterial, graphene oxide (GO), can also serve as a multifunctional platform for gene delivery, imaging, and cancer sensing [111]. The GO surface can be modified with positively-charged moieties in order to ensure siRNA loading [112, 113]. For instance, conjugated with cationic material (chitosan) and loaded with siRNA, graphene oxide shows down-regulation of the target mRNA and protein level in MCF-7 cells, producing a significant antitumor effect *in vivo* [113]. While all aforementioned nanomaterials can be prospective platforms for siRNA delivery, their toxicity at low concentrations, long-term tissue accumulation, and complex synthesis [114, 115] can limit them from proceeding to mass production and clinical studies.

As it was shown earlier, another carbon nanomaterial, graphene quantum dots (GQDs), has emerged as a promising carrier for gene delivery [1, 2]. It was found that the microwave-assisted method for GQDs synthesis shortens the time for synthesis and can be used with different carbon precursors that enrich GQDs with dopants and expand the functions of GQDs. For example, a previous graduate student, currently Dr. Campbell, used a glucosamine-HCL solution as a carbon precursor in order to enrich GQDs with amine groups for the facilitation of gene transfection [65] making this nitrogen-doped GQDs (NGQDs) a promising vehicle for siRNA delivery. In addition to being a delivery agent, GQDs can be also utilized for imaging and biosensing. They are photostable and exhibit intrinsic fluorescence in the visible (VIS) and NIR, which can serve as a non-invasive detection mechanism [4, 5]. In our previous work, we assessed the visible fluorescence quantum yield (QY) of NGQDs by using a relative method with the use of Coumarin-153 and Fluorescein as two standard materials with excitation and emission wavelengths similar to NGQDs. Both standards show similar results

with estimated QY ranging from 50 to 60% for NGQDs [70]. Such high quantum yield can be advantageously utilized for *in vitro* applications.

Enhancing GQD biocompatibility and image-tracking modalities can facilitate the progression of the GQD platform toward *in vivo* applications. The use of NIR rather than visible fluorescence is paramount in deeper-tissue imaging since visible light experiences greater tissue scattering and absorbance rather than near-infrared within so-called biological windows. These windows represent three distinctive wavelength regions: 700 to 950 nm (NIR-I), 1000 to 1350 nm (NIR-II), and 1550 to 1870 nm (NIR-III) [116]. While visible fluorescence of GQDs mostly arises from the quantum-confinement effect, functional groups and defect sites contribute to long-wavelength fluorescence, including near-infrared [70]. However, utilization of NIR emission of GQDs is hampered by their low fluorescence quantum yield and 850 nm emission that is located at the edge of the CCD and InGaAs cameras' detection windows [65]. In our previous work, we synthesized GQDs from reduced graphene oxide (RGQDs) with a top-down approach [117] that exhibit fluorescence in NIR at the peak of ~950 nm. Using an absolute method of measuring quantum yield, the QY of RGQDs is measured as $6.29 \pm 0.5\%$ and $1.34 \pm 0.15\%$ with 637 nm and 808 nm excitation, respectively. This value is higher as compared to other reported quantum dots and SWCNTs [118-120]. Although RGQDs are a promising nanocarrier with NIR imaging capabilities, it is likely not suitable for siRNA loading as they have a negatively charged surface with a zeta potential of -4.69 ± 0.90 mV.

In order to modify GQDs' optical properties toward the desired NIR emission and keep GQDs positively charged, doping with rare-earth metal ions can be utilized [121, 122]. Rare-earth elements constitute a class of lanthanide ions found in the 6th row of the periodic table. Due to the incompletely filled 4f shell that is shielded by their outer-shell electrons and whose

energy levels undergo splitting mechanisms, lanthanides possess extremely complex optical properties [123]. One of these properties is luminescence that for the trivalent lanthanide ions (Nd^{3+} , Er^{3+} , Yb^{3+} , and Tm^{3+}) arises from f-f transitions of the 4f shell and f-d transitions in the 4f-5d shell. The f-f transitions provide the lanthanide elements with rich energy level structures in the NIR range [124]. Rare earth-based nanoparticles already showed their high photostability, deep tissue penetration [125, 126], and high quantum yields of up to 32% depending on the structure [127]. However, the obstacles in core/shell structure synthesis and increased size are making it difficult for the nanoparticles to gain entry into biological tissues and keeping rare-earth metal-based nanomaterials away from clinical trials.

Encouraged by the success of coordination chemistry, scientists introduced rare-earth metal ions into ligands and developed NIR lanthanide complexes. While the idea of using coordination chemistry is remarkable, these complexes are still far away from use in clinics due to their complex and not cost-effective synthesis, toxicity, and poor solubility in water [122]. Given the successful prior development of biocompatible and water soluble nitrogen-doped graphene quantum dots, we utilize doping with neodymium ions to modify their imaging properties toward the desired NIR-II biological window (Figure 5). In fact, the NIR fluorescence arising from Nd dopants in Nd-NGQDs can be successfully utilized for *in vivo* animal imaging of live mice without their dissection.

Therefore, nitrogen-containing and neodymium-doped graphene quantum dots (NGQDs and Nd-NGQDs, respectively) possess desired capabilities of cost-effective synthesis, gene loading, and imaging in visible, as well as near-infrared spectral regions [65, 121]. They are biocompatible at high concentrations and exhibit fluorescence in visible and near-infrared spectrum regions. NGQDs having nitrogen functional groups on their surface

show the capacity for non-covalent gene attachment forming stable complexes with adsorbed ssDNA [8]. These properties suggest that NGQDs and Nd-doped NGQDs can serve as perspective platforms for image-guided siRNA delivery.

To test this, we have for the first time utilized biocompatible NGQDs and Nd-NGQDs for the delivery and imaging of KRAS and EGFR siRNAs in HeLa cells. Unlike previously developed platforms for siRNA delivery, NGQDs and Nd-NGQDs are synthesized by a one-step microwave-assisted hydrothermal method that does not contain any substantially toxic precursors, thereby rendering these GQDs biocompatible and simple in production. Moreover, NIR fluorescent GQDs that can offer the advantage of *ex vivo* and *in vivo* tracking have not been previously utilized for gene delivery or imaging. This work, therefore, explores unique anticancer therapeutic siRNA delivery platforms that possess a promising potential for translating siRNA technology into clinics.

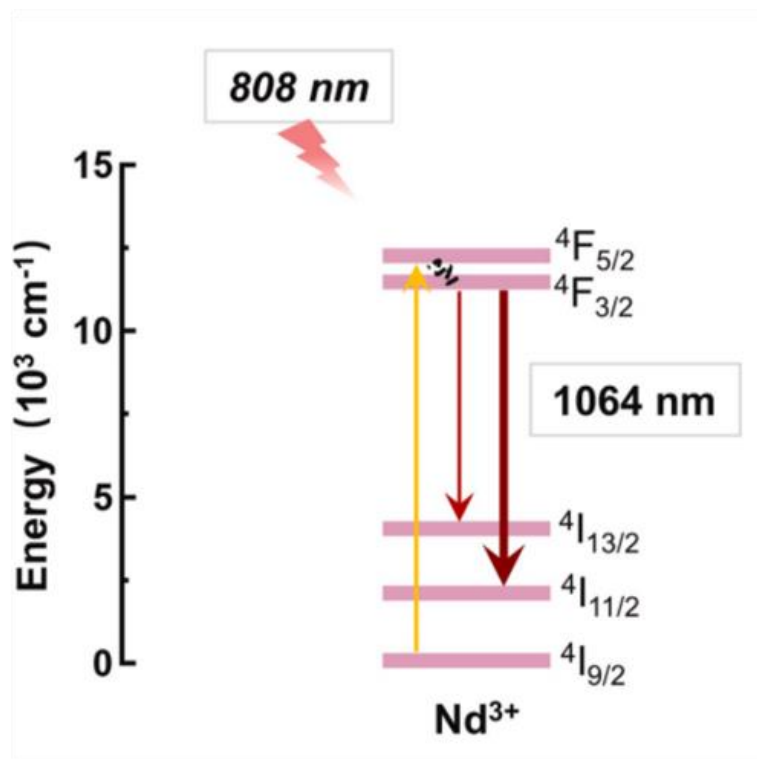


Figure 5. 808 nm excited Nd³⁺ system, and the corresponding mechanisms for NIR emission [128].

2. Experimental Methods and Equipment

2.1. Synthesis of NGQDs and Nd-NGQDs

In order to produce nitrogen-doped graphene quantum dots (NGQDs) and neodymium-doped graphene quantum dots (Nd-NGQDs), 4 g of glucosamine hydrochloride (104K0082, Sigma-Aldrich) was dispersed in 250 mL of deionized (DI) water. For Nd-NGQDs (Figure 6), 0.008 M aqueous solution of $\text{Nd}(\text{NO}_3)_3 \cdot 6\text{H}_2\text{O}$ (MKCH8576, Sigma-Aldrich) was added. The mixture was microwaved in the HB-P90D23AP-ST Hamilton Beach microwave oven for 60 min at a 1350 W power level. After the synthesis, samples were cooled down and transferred to a 1 kDa molecular weight cutoff dialysis bag for 24 h dialysis against DI water to remove unreacted material. DI water was changed every 30 min for the first 3 h, and every 7 h for the next 21 h. Then, all the samples were sterilized using a 0.22 μm syringe filter. The dialyzed and sterilized products were further used in the aqueous suspension form.

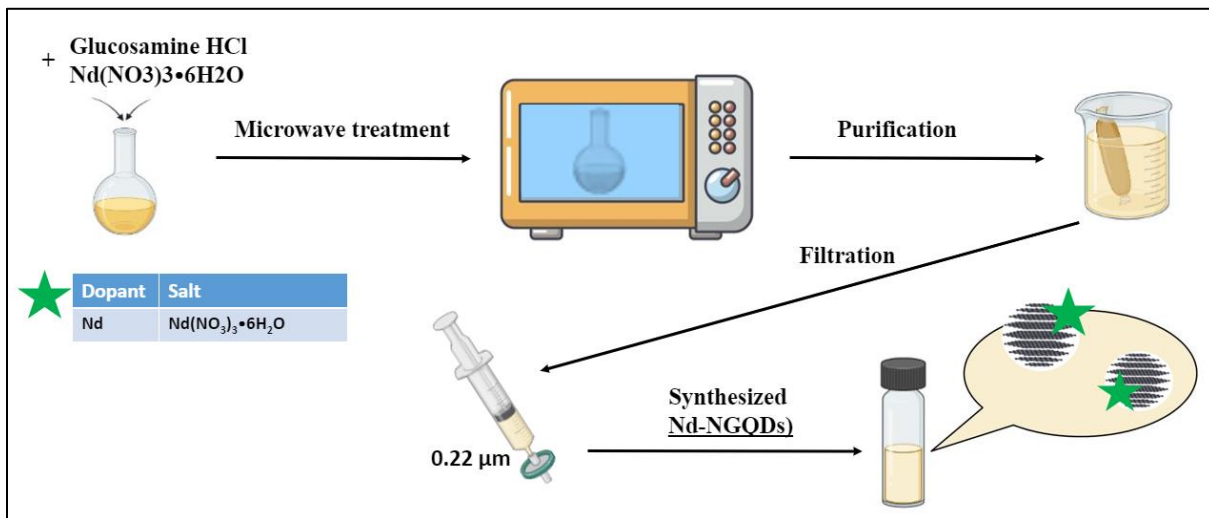


Figure 6. The schematic of Nd-NGQDs synthesis.

2.2. Complexation of NGQDs and Nd-NGQDs with siRNAs

To load siKRAS and siEGFR (Nitto AVECIA) onto both types of GQDs, 750 μg of GQDs in aqueous suspension were mixed with 0.5, 1, 5, 10, and 15 μL of siKRAS or siEGFR stock solution (1 nmol/ μL in DEPC treated water) and incubated for 10 min at room temperature to produce GQD/siRNA complexes at 1:0.01, 1:0.02, 1:0.1, 1:0.2 and 1:0.3 weight ratios.

2.3. Structural Characterization

Confirmation of the size distribution of NGQDs, Nd-NGQDs and NGQD/siEGFR complex and chemical composition of Nd-NGQDs was performed by HRTEM (high-resolution transmission electron microscopy, JEOL JEM-2100) with energy dispersive X-ray analysis (EDS, JEOL, Peabody, MA, USA). The samples were air-dried on the carbon-coated 200-mesh copper grid. To assess the functional groups of NGQDs and Nd-NGQDs, the samples were analyzed via the ATR mode of the Thermo Nicolet Nexus 670 FTIR after freeze-drying in the Labconco FreeZone 4.5 freeze-dryer.

The structure of the NGQD/siEGFR complexes was investigated by the energy minimization method through the auto-optimization tools within Avogadro software [129]. Merck Molecular Force Field 94 (MMFF94) [130] was chosen as it is best utilized with organic materials such as NGQDs and siRNA. Moreover, the steepest descent optimization algorithm was used with an energy convergence of 10^{-6} units at a 2500-step limit to provide the best structural assessment. The center flake of the multi-layer NGQDs was built in accordance with previous theoretical modeling of the NGQD structures based on percentages of oxygen and nitrogen-containing functional groups [70]. Other GQD planes were derived from the central and separately optimized before going through a final geometrical optimization with the

siRNA. The exact siEGFR sequence used for fluorescence imaging in this work is presented in the model.

2.4. Optical Characterization

The absorbance of NGQDs and Nd-NGQDs was measured within the range of 200–1000 nm with Agilent Technologies (Cary 60 UV–vis) absorption spectrometer. Photoluminescence spectra of NGQDs and Nd-NGQDs in the visible and NIR regions were measured utilizing Horiba Scientific SPEX NanoLog. Fluorescence microscopy measurements were performed using an Olympus IX73 fluorescence microscope with a 60× (IR-corrected Olympus Plan Apo) water immersion objective and Photometrics Prime 95B CMOS camera coupled to Olympus DSU (disk spinning unit) confocal system for visible imaging with excitation/emission filter wheels enabling spectrally resolved image acquisition. An optimal configuration of filters is selected based on GQD (480 ± 20 nm excitation and 535 ± 20 nm emission filters) and ROX (540 ± 20 nm excitation and 605 nm emission filters) emission spectra. The fluorescence microscope is coupled to the NIR InGaAs Photon etc. (ZephIR 1.7) detector through the hyperspectral fluorescence imager (Photon etc.), enabling spectrally resolved imaging in the near-infrared region (850–1600 nm).

2.5. Electrokinetic Characterization

In order to estimate the electrophoretic properties of the GQD/siRNA complex and find the best complexation ratio between GQDs and siRNA, gel retardation assay was used. siEGFR and siKRAS were mixed with NGQDs and Nd-NGQDs water suspensions at various weight ratios, maintaining the concentration of siEGFR and siKRAS constant. The resulting samples were incubated for 10 mins, mixed with 1X BlueJuice™ DNA loading buffer (10816015,

Invitrogen), loaded onto 1.75% (w/v) agarose gel, and run in Tris-Borate-EDTA (TBE) buffer at 80 V for 45 min. After electrophoresis, gels were stained in 0.5 µg/mL ethidium bromide solution (20F1056078, Invitrogen) in TBE buffer for 20 minutes on an orbital shaker. To reduce the background signal, the agarose gel was destained in TBE buffer for 5 minutes on an orbital shaker after which all the gels were imaged using FastGene® FAS-V Imaging System. In order to evaluate the net charge of GQDs and their complexes with siRNA Zeta potential of GQDS and NGQD/siEGFR, NGQD/siKRAS, Nd-NGQD/siEGFR and Nd-NGQD/siKRAS complexes at 1:0.01 w/w ratios were measured using NanoBrook ZetaPALS instrument.

2.6. Cell studies

The HeLa cells were cultured in Dulbecco's modified Eagle medium (D6046, Sigma-Aldrich), 10% fetal bovine serum (16140-063, Gibco) with the addition of 1% l-glutamine (G7513, Sigma-Aldrich), minimum essential medium (MEM) non-essential amino acid solution (M7145, Sigma-Aldrich) and penicillin/streptomycin (P4333, Sigma-Aldrich). The cell culture was kept in an incubator with 5% CO₂ at 37°C and used for the cell viability assay, cell internalization microscopy study, and western blot analysis.

Biocompatibility of GQDs was established by performing a cell viability assay. HeLa cells were plated at 5×10^3 cells per well in a 96-well plate and allowed to attach overnight. The cells were further treated with NGQD/siEGFR, NGQD/siKRAS, Nd-NGQD/siEGFR or Nd-NGQD/siKRAS at the weight ratio of 1:0.01 with different concentrations of NGQDs and Nd-NGQDs. After 48 h incubation, the medium was replaced by 100 µL of 1 mg/mL 3-(4-dimethylthiazol-2-yl)-2,5-diphenyltetrazolium bromide (MTT). After 4 h of further

incubation, MTT was replaced with 100 μ L of dimethyl sulfoxide (DMSO) to dissolve blue formazan formed in the metabolically active cells. The characteristic formazan absorbance was measured on a microplate reader (FLUOstar Omega) at 580 nm and considered proportional to the number of alive cells.

Cell internalization microscopy experiment assesses the internalization of NGQD/siRNA or Nd-NGQD/siRNA hybrids at 375 μ g/mL GQD concentrations and 1:0.01 weight ratios with carboxy-X-rhodamine (ROX)-tagged siEGFR (5'-GUCGCUAUCAAGGAAUUAAdTdT-3') and siKRAS (5'-CGAAUAUGAUCCAACAAUAdTdT-3') genes. HeLa cells were seeded at 1×10^4 cells onto a glass coverslip placed in a 6-well plate overnight. The cells were treated with NGQD/siEGFR-ROX, NGQD/siKRAS-ROX, Nd-NGQD/siEGFR-ROX or Nd-NGQD/siKRAS-ROX for 12 h. The coverslips with cells were further washed with 1X phosphate-buffered saline (PBS) to remove GQD/siRNA complexes that did not internalize. Cells were fixed with 4% formaldehyde solution (28908, Thermo Scientific) and $1 \times$ Fluoromount-GTM mounting medium (00-4958-02, Invitrogen), and sealed onto microscope slides for imaging with Olympus IX73 fluorescence microscope with aforementioned visible and NIR detection systems.

In order to estimate protein knockdown with GQD/siRNA complex western blot assay was utilized. HeLa cells were plated at 1.8×10^5 cells per well in a 6-well plate and allowed to attach overnight. The cells were transfected with NGQD/siEGFR, NGQD/siKRAS, Nd-NGQD/siEGFR, or Nd-NGQD/siKRAS at different ratios following the procedure from section 2.2, as well as with Lipofectamine 3000 (L3000001, Invitrogen) delivering siKRAS or siEGFR as per the manufacturer's protocol. After 24 h cells were washed with fresh complete

medium and left for an additional 24 hours of incubation. After that, the cells were washed with room temperature phosphate-buffered saline (PBS) and directly lysed in RIPA lysis buffer (20-188, Millipore Sigma) supplemented with protease and phosphatase inhibitor cocktails (11836153001 and 04906845001, Roche). All the proteins were extracted and quantified by the Bradford protein assay using bovine serum albumin (BSA) as a standard. The proteins were further mixed with SDS Loading Buffer (BioRad) and heated for 10 min at 95°C. Equal amounts of protein were electrophoresed in 10% TGX Stain-Free acrylamide gel (1610182, BioRad) at 100 V for 1.5 hours and transferred onto a nitrocellulose membrane (88018, Thermo Scientific) at 25 V and 1.0-1.3 A using the Trans-Blot Turbo transfer system apparatus (1704150, BioRad). Membranes were blocked with blocking buffer (3% BSA in TBS-T (Tris-buffered saline with 0.1% Tween® 20 detergent, Biorad)) for 1 hour and incubated with primary antibodies (Actin, Santa Cruz Biotech sc-8432, 1:1000 dilution; KRAS, sc-30, 1:200 dilution; EGFR, sc-365829, 1:200 dilution) in the blocking buffer overnight at 4°C. After that, membranes were washed with blocking buffer three times and incubated with a secondary antibody (1706516, Biorad, 1:3000 dilution) for 1-2 h. Actin was used as a control, to ensure that an equal amount of protein was loaded in each line. After washing, membranes were stained with Opti-4CN Substrate Kit (1708235, Biorad) and imaged using FastGene® FAS-V Imaging System.

3. Results and discussion

Are graphene quantum dots suitable for siRNA delivery with imaging capabilities?

3.1. Size characterization

In this work, a novel avenue for siRNA cancer gene therapy is explored with NGQD and Nd-NGQD carrier/imaging platforms synthesized utilizing a microwave-assisted hydrothermal method with glucosamine carbon precursor. Upon microwave treatment, glucosamine molecules undergo hydrothermal reaction and form aromatic clusters, serving as nucleation centers for the formation of NGQDs. With the addition of $\text{Nd}(\text{NO}_3)_3 \cdot 6\text{H}_2\text{O}$ salt into the reaction mixture, neodymium ions dope the nucleating NGQDs yielding the formation of Nd-NGQDs. The morphology and structure of the purified and filtered NGQDs and Nd-NGQDs are characterized by TEM and HRTEM. Both samples contain evenly distributed GQDs with respective average diameters of 4.0 ± 0.6 nm and 3.8 ± 0.9 nm (Figure 7 (a-b)). HRTEM images (Figure 7(c-d)) of NGQDs and Nd-NGQDs reveal their graphitic structure demonstrating characteristic graphene lattice fringes [131] with 0.26 ± 0.03 and 0.21 ± 0.03 nm respective interplanar spacing, while the fast Fourier transform (FFT) images confirm their crystallinity. EDX analysis is performed to ensure the presence of Nd in Nd-NGQDs after purification and filtration removing unreacted Nd precursors (Figure 7(e)). EDX spectrum demonstrates ~1 atomic percent of Nd in Nd-NGQDs confirming their successful doping. Due to its small amount, the metal dopant is not expected to affect the biocompatibility of the GQDs [132]. Besides Nd, EDX analysis indicates carbon, oxygen, and nitrogen suggesting the presence of various functional groups in the GQD structure.

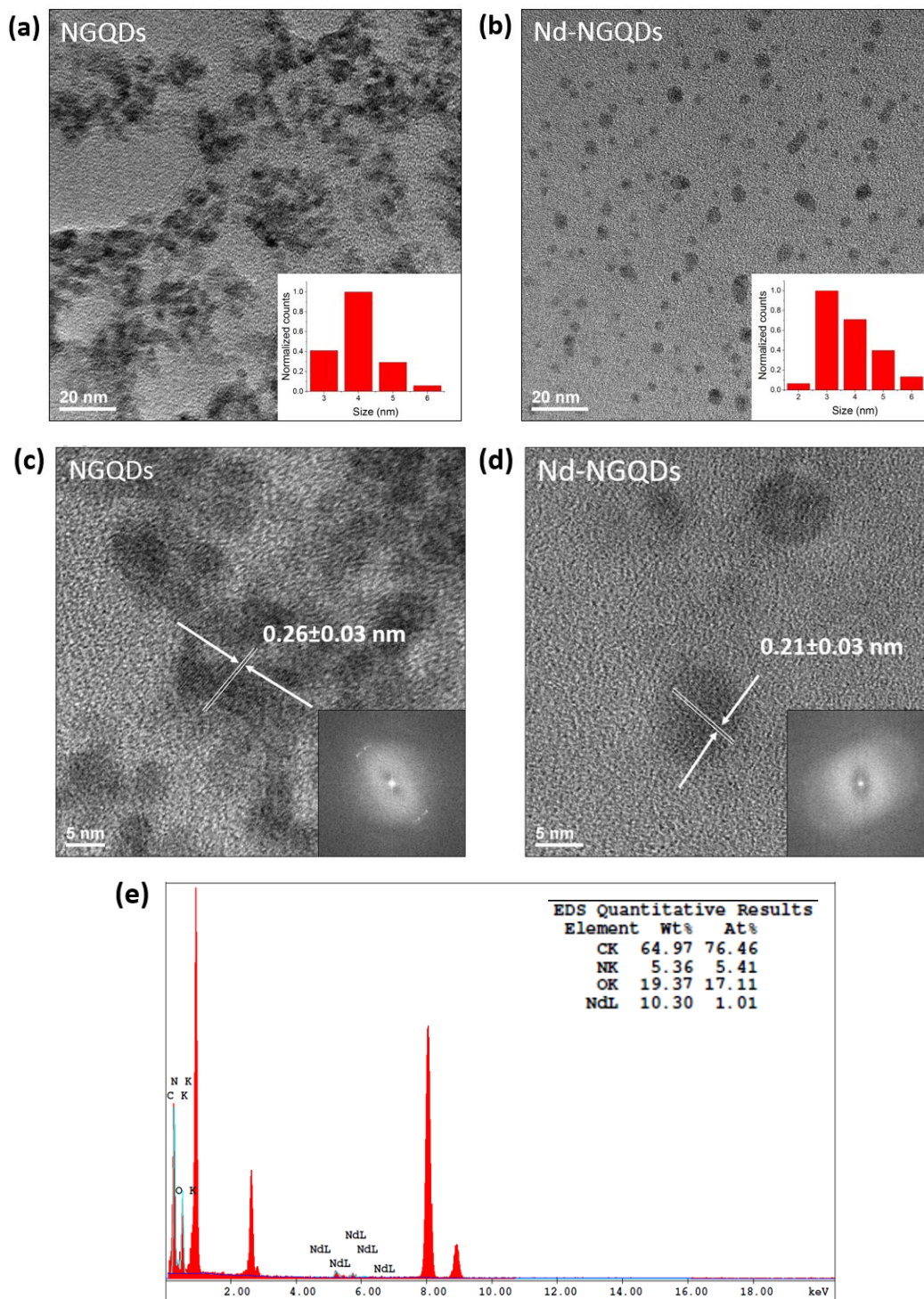


Figure 7. TEM images and size distributions of (a) NGQD (4.0 ± 0.6 nm) and (b) Nd-NGQDs (3.8 ± 0.9 nm). HRTEM images of NGQDs (c) and Nd-NGQDs (d) with corresponding characteristic graphitic lattice spacings. Inset: FFT image. (e) EDX spectra of Nd-NGQDs. Inset: Weight/atomic percentages of Carbon, Nitrogen, Oxygen and Neodymium.

FTIR of freeze-dried GQD samples (Figure 8) identifies hydroxyl, carboxyl, and amino groups most likely present on the surface of the GQDs enabling high water solubility as well as complexation with nucleic acids [8] and covalent functionalization for biological applications [133]. In this work, several modalities of these GQD platforms are tested to identify their capability for successful siRNA delivery.

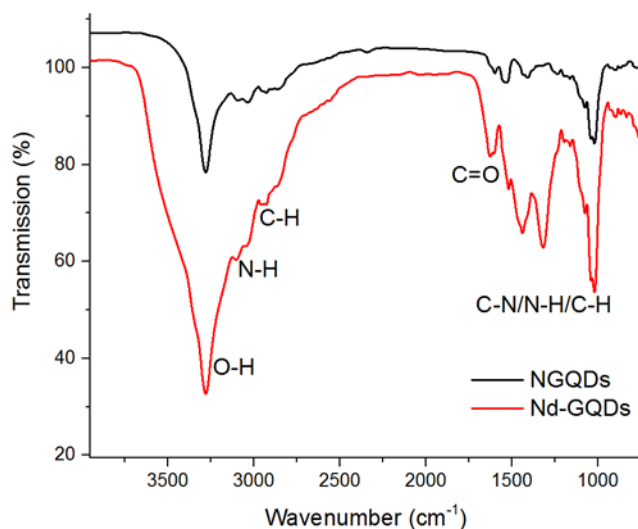


Figure 8. FTIR spectra of NGQDs and Nd-NGQDs. NGQDs spectrum is shifted up by 10 % for visualization.

3.2. Optical properties

In order to assess the imaging capabilities of the GQD platforms, their optical properties are evaluated via absorbance and fluorescence spectroscopies. Absorption spectra of NGQDs and Nd-NGQDs (Figure 9 (a)) show dominant features at ~ 200 nm and ~ 276 nm that are ascribed to $\pi-\pi^*$ and $n-\pi^*$ electronic transitions of the C=C and C=O bonds, respectively. The shoulder at ~ 317 nm is attributed to the $\pi-\pi^*$ transition of the C=N bond [134]. Nd-NGQDs also possess an absorption peak at ~ 800 nm (Figure 9 (b)) corresponding to the $^4I_{9/2} \rightarrow ^4F_{5/2}$ transition of the Nd^{3+} , enabling their fluorescence excitation with an 808 nm laser.

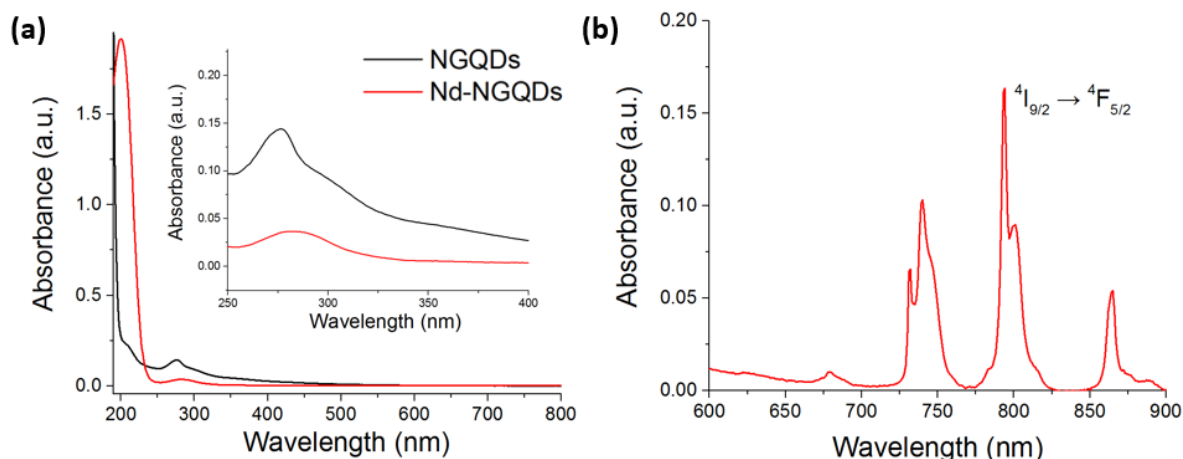


Figure 9. (a) UV-VIS absorption spectra of NGQDs and Nd-NGQDs. (b) NIR absorption spectra of Nd-NGQDs at 10 mg/mL concentration.

With this excitation Nd-NGQDs exhibit several emission features at ~900, 1060, and 1330 nm (Figure 10 (a)) attributed to the ${}^4F_{3/2} \rightarrow {}^4I_{9/2}$, ${}^4F_{3/2} \rightarrow {}^4I_{11/2}$ and ${}^4F_{3/2} \rightarrow {}^4I_{13/2}$ neodymium(III) electronic transitions, verifying the capability of Nd-NGQDs for deep tissue NIR imaging [121]. Both NGQDs and Nd-NGQDs exhibit fluorescence in the visible region (Figure 10 (b)). Excited with 400 nm, both samples show a similar broad emission peak at ~500 nm ascribed to the quantum confinement-originating intrinsic GQD fluorescence [70]. The width of the spectrum is attributed to the distribution of different GQD sizes in the sample with a variety of size-dependent emission wavelengths. While visible fluorescence is not commonly used for *in vivo* applications, it provides an essential *in vitro* imaging modality enabling tracing the internalization of the GQDs into biological cells. Overall, the visible and NIR fluorescence capabilities of NGQDs and Nd-NGQDs make them prospective nanomaterials for bioimaging applications *in vitro* and *in vivo*.

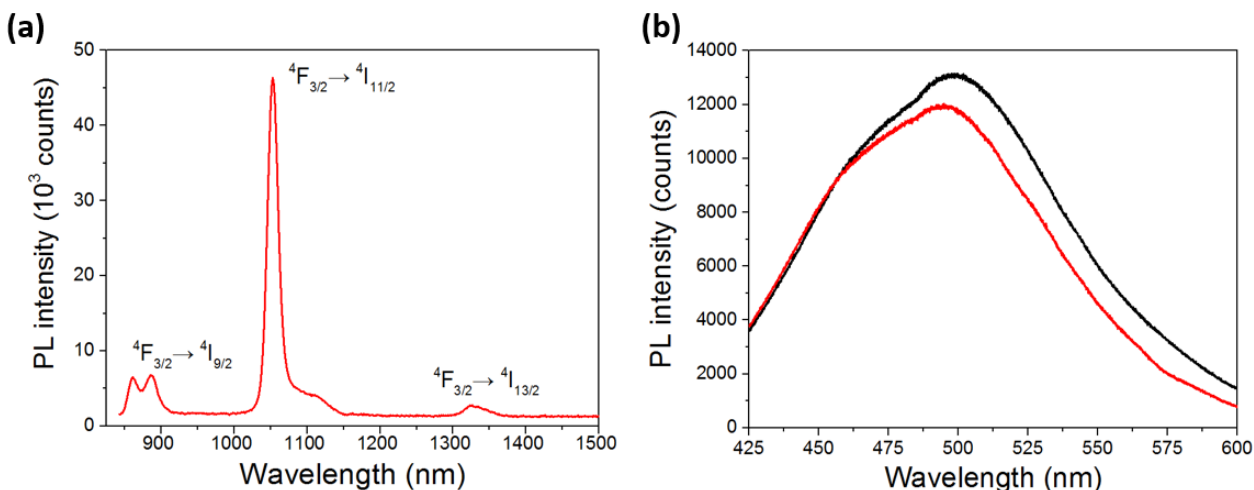


Figure 10. (a) NIR fluorescence of Nd-NGQDs at the concentration of 11.3 mg/mL with 808 nm laser excitation. (b) Visible fluorescence of NGQDs (black) and Nd-NGQDs (red) at 10 and 11.3 mg/mL concentrations with 400 nm xenon lamp excitation.

3.3. GQD/siRNA complex characterization

The capabilities of NGQDs and Nd-NGQDs to complex siRNA for its delivery were assessed via zeta potential and gel retardation assays. Both NGQDs and Nd-NGQDs show positive zeta potentials (1.8 ± 0.7 mV and 8.3 ± 0.7 mV respectively), indicative of their positive surface charge (Figure 11) attributed mainly to amino groups on the GQD surface. The incorporation of Nd^{3+} into the Nd-NGQD structure and positive defects created by doping can be deemed responsible for the elevated zeta potential of the Nd-NGQDs [135]. Utilizing positively-charged GQDs can facilitate more effective binding of the siKRAS and siEGFR genes that possess negative zeta potentials (-18.8 ± 1.4 mV and -9.9 ± 0.8 mV, respectively) and are negatively charged due to the presence of phosphate groups. Given this electrostatic binding advantage, the loading capacity of both genes onto NGQDs and Nd-NGQDs was evaluated via the gel retardation assay (Figure 12). In this assay, each GQD type and each gene are mixed together in an aqueous suspension at the weight ratios of 0:1, 1:2, 1:1, 3.3:1, 5:1,

10:1, 50:1, and 100:1, and incubated for 10 minutes at room temperature to allow complexation. When loaded onto the gel, the complex with lower mobility is likely to be more neutral, which is expected from a most efficient combination of positively charged GQDs and negatively charged siRNA [136]. The results of the gel retardation assay demonstrate that the migration of siEGFR and siKRAS gradually decreases with increasing of GQD/siRNA ratio. The maximum band “shift” with respect to the control column (0:1), which contains only negatively-charged siRNA, was observed at GQD/siRNA weight ratio of 100:1 indicating efficient complexation of siRNAs and GQDs at this ratio. The zeta potential of the Nd-NGQD/siEGFR and Nd-NGQD/siKRAS at that weight ratio is measured to be positive (0.8 ± 0.3 mV and 5.1 ± 0.6 mV, respectively), giving a promise for effective cell entry and endosomal escape [137]. NGQD/siEGFR and NGQD/siKRAS demonstrate negative zeta potential (-6.9 ± 0.6 mV and -4.4 ± 1.1 mV) due to the initially lower charge of the NGQDs with the same amount of siRNA complexed. Similar potentials were previously observed for the NGQD platform with absorbed single-stranded DNA for miRNA detection [8].

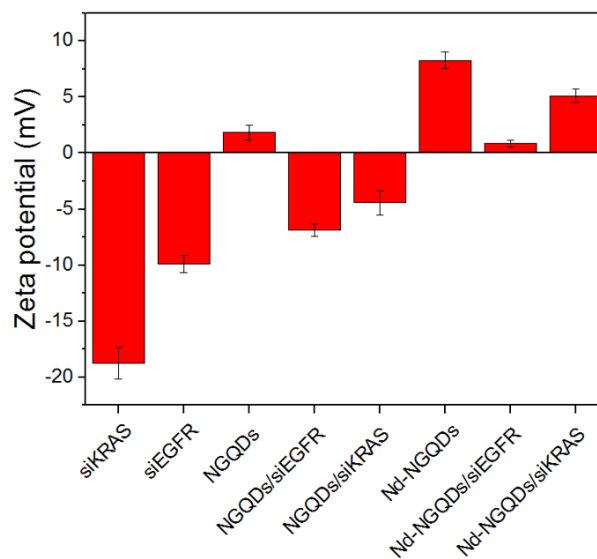


Figure 11. Zeta potential of siKRAS, siEGFR, NGQDs, Nd-NGQDs and NGQD/siEGFR, NGQD/siKRAS, Nd-NGQD/siEGFR and Nd-NGQD/siKRAS complexes at 1:0.01 w/w ratio.

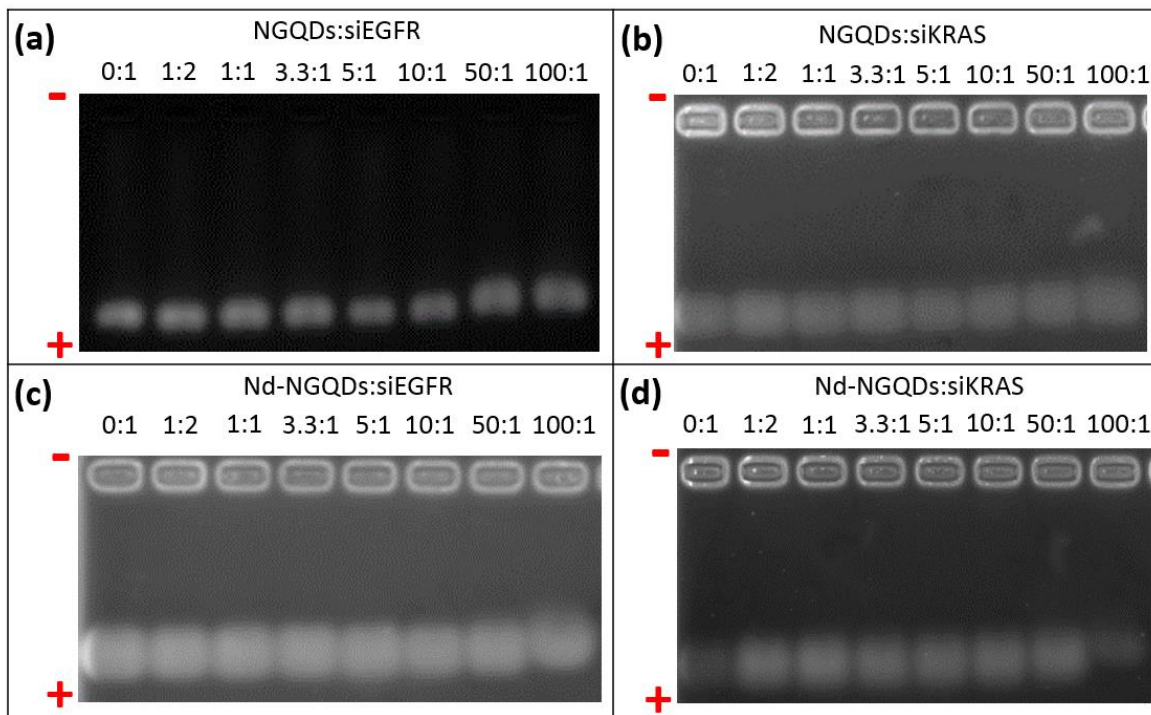


Figure 12. Gel retardation assay of (a) NGQD/siEGFR, (b) NGQD/siKRAS, (c) Nd-NGQD/siEGFR, (d) Nd-NGQD/siKRAS complexes at different w/w ratios.

The change in the net electric charge of all complexes confirms the electrostatic interaction between the GQDs and siRNA. While having positively-charged nanoparticles may pose a substantial advantage for internalization, negatively-charged GQDs appear to enter the cells via an entirely different internalization mechanism [138]. In the case of cationic GQDs, micropinocytosis is considered a major internalization pathway, while anionic GQDs are known to internalize mostly through caveolae-mediated and clathrin-mediated endocytosis [138, 139]. Micropinocytosis involves the formation of large uncoated vesicles, where clathrin-mediated endocytosis bring nanoparticles into a cell within a clathrin-coated vesicle, and caveolae-mediated endocytosis induces the formation of flask-shaped vesicles that is the result of the interaction with caveolin protein. Thus, despite their charge, both NGQD/siRNA and Nd-NGQD/siRNA complexes have a potential for gene delivery.

Following up on the zeta potential results, we performed geometry optimization calculations with the MMFF94 force field (Figure 13) that demonstrates a plausible configuration of the NGQD/siEGFR complex. Electrostatic interaction between the GQDs and the gene can arise from the alignment of positively charged at biological pH amino groups of the NGQDs and negatively charged siRNA phosphate groups (Figure 4, Inset). The calculation shows the potential of successfully complexing several GQD structures with the larger siRNA sequence. Experimentally, HRTEM and TEM images of NGQD/siEGFR complexes show bigger structures compared to individual GQDs as expected from the simulation, indicating successful siEGFR adsorption onto NGQD surface (Figure 14). After complexation assessment, different weight ratios are further tested for gene delivery in HeLa cells.

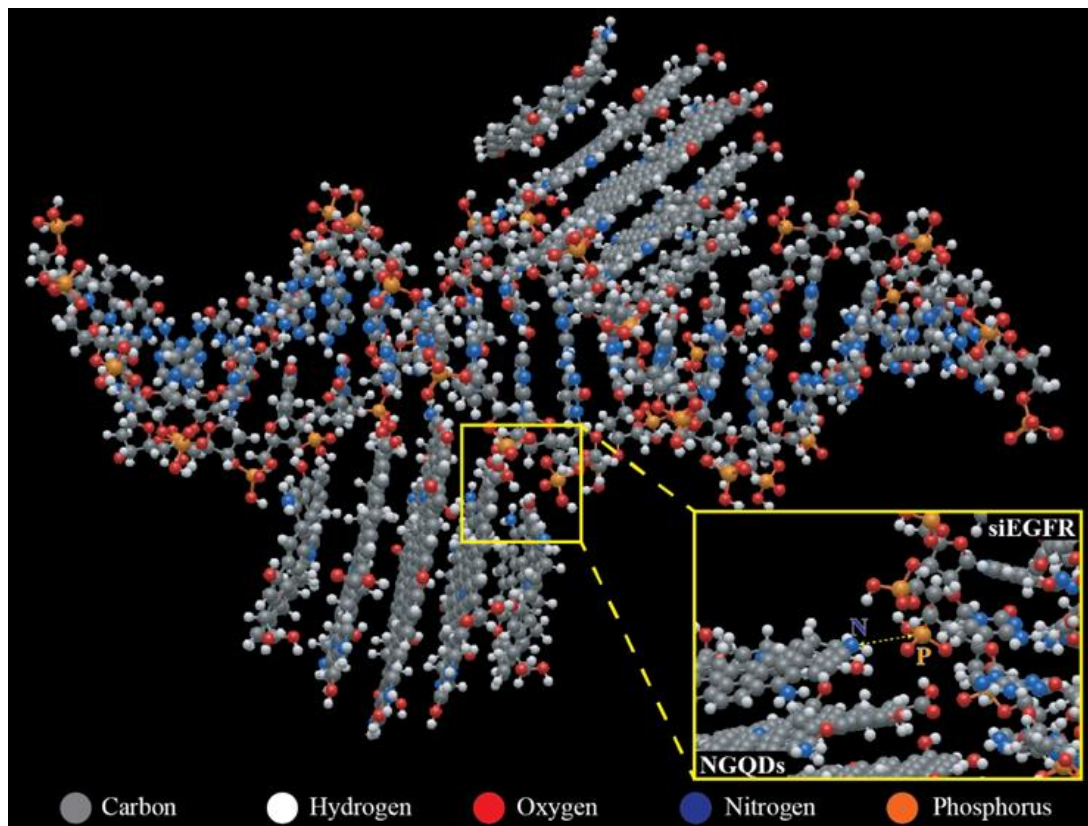


Figure 13. Molecular visualization of NGQD/siEGFR complex geometrically optimized with MMFF94 energy minimization calculation. Inset: zoomed-in area showing the proximity of NGQD amine siEGFR phosphate groups.

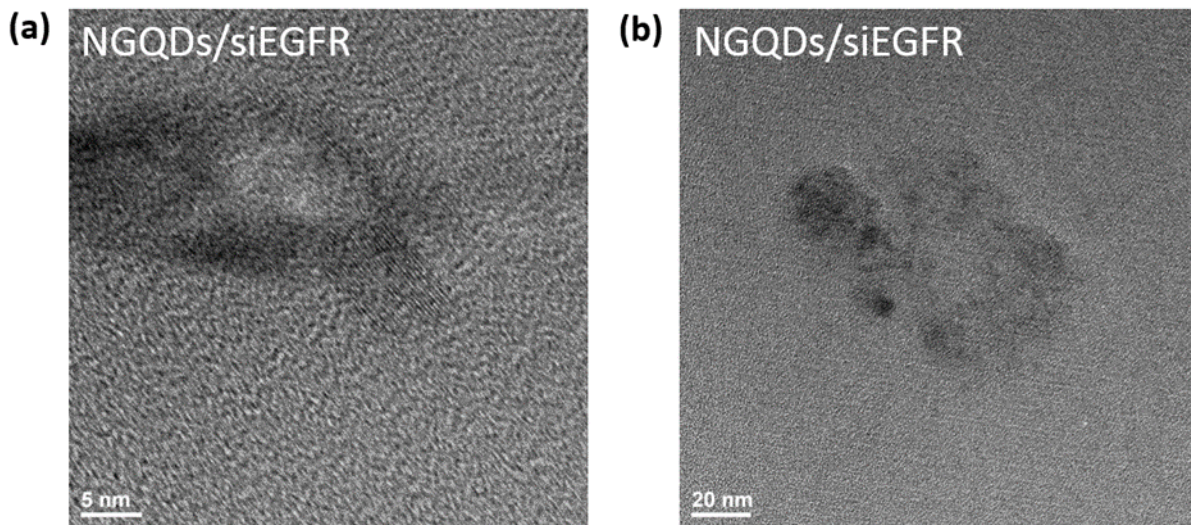


Figure 14. (a) HRTEM and (b) TEM images of NGQD/siEGFR complex at 1:0.01 weight ratio.

3.4. Cell Viability

Maximum biocompatible concentrations for intracellular delivery of siRNA are determined in this work via the MTT cytotoxicity assay. Due to the low cytotoxicity of the precursor material and only small percent metal doping, both NGQDs and Nd-NGQDs are expected to exhibit biocompatibility at high concentrations. In order to select the highest biocompatible concentration for imaging and delivery, HeLa cells were treated with NGQD/siEGFR, NGQD/siKRAS, Nd-NGQD/siEGFR, and Nd-NGQD/siKRAS complexes for 48 hours at different amounts of NGQDs and Nd-NGQDs (Figure 15 (a) and (b)). Both complexes demonstrate ~70-80 % cell viability at 375 $\mu\text{g/mL}$, indicating that minor Nd doping does not contribute to the toxic profile of the formulation.

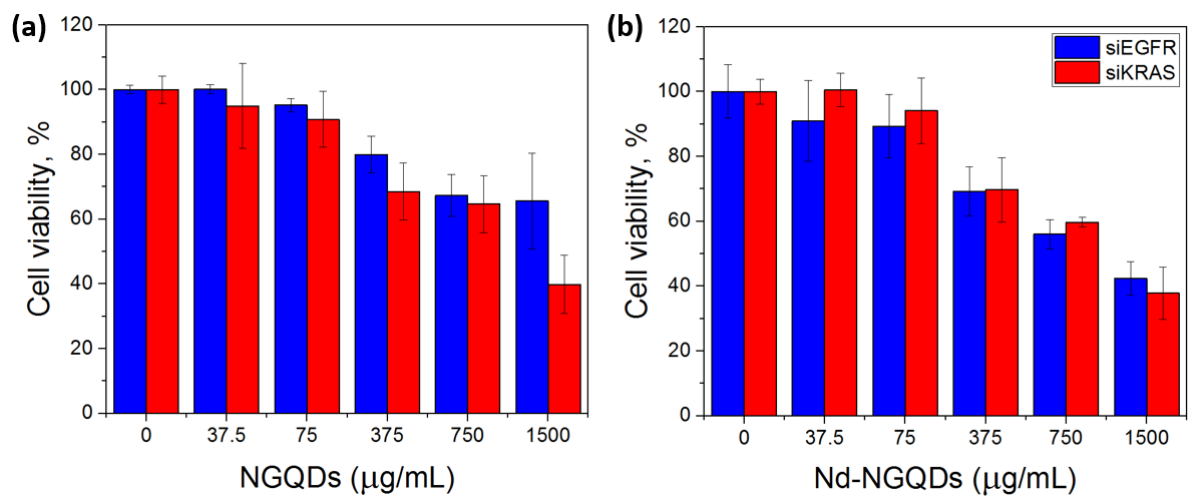


Figure 15. Cell viability of HeLa cells after treatment with (a) NGQD/siEGFR and NGQD/siKRAS, (b) Nd-NGQD/siEGFR and Nd-NGQD/siKRAS complexes at 1:0.01 weigh ratio.

Can GQD/siRNA complexes be used for imaging in vitro?

3.5. Internalization/excretion study of GQDs

In order to track GQDs inside the cells and assess the optimal timeline for imaging, a fluorescence-based internalization/excretion study is performed via *in vitro* fluorescence microscopy. While 12 h has been previously determined as an optimal internalization time for NGQDs [65], here, we performed an internalization/excretion study for Nd-NGQDs utilizing their optical properties. Based on the Nd-NGQDs VIS fluorescence, emission within the cells is recorded with 460 nm filtered lamp excitation and 540 nm filtered emission. Nd-NGQDs were introduced into the HEK-293 cells and incubated for 1, 6, 12, 24, and 48 h. The fluorescence intensity per cell area is used as a measure of internalization/excretion dynamics of the nanomaterial in the HEK-293 cells over time (Figure 16 (a)).

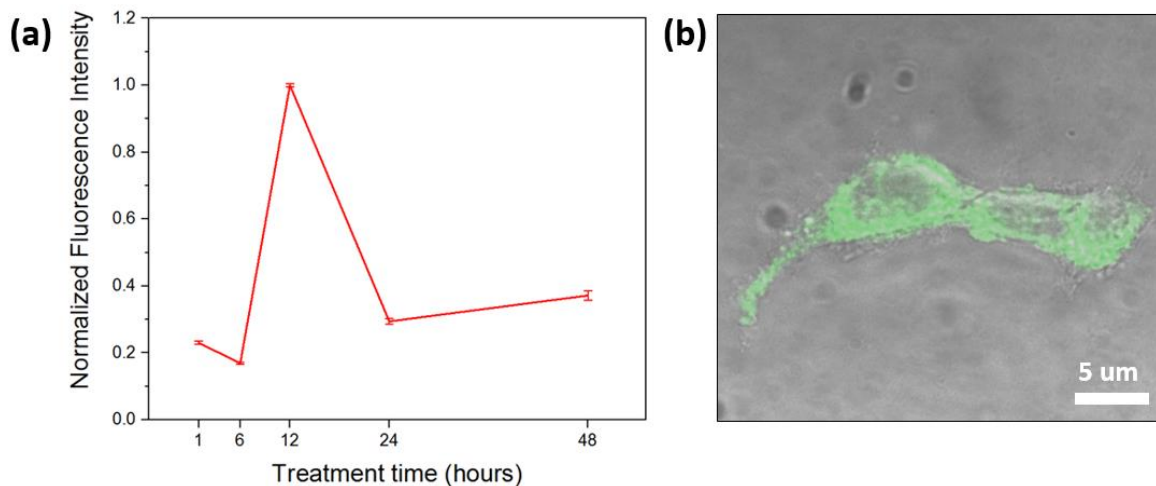


Figure 16. (a) Cellular internalization/excretion dynamics of Nd-NGQDs samples over 1, 6, 12, 24, and 48 h based on the fluorescence intensity of Nd-NGQDs within the HEK-293 cells in the VIS (460 nm excitation, 540 nm emission). (b) Bright-field/VIS fluorescence confocal overlay images of HEK-293 cells treated with Nd-NGQDs at their optimal internalization time point of 12 hours.

Such imaging accounts only for the Nd-NGQDs that are internalized since the ones remaining in the intracellular space are removed by a washing step during slide preparation. In order to quantify the internalization, the Nd-NGQDs emission from over 200 cells is analyzed at each time point, and the average intensity per unit cell area is then used as a measure of the intercellular Nd-NGQDs concentration. This analysis (Figure 16 (a)) demonstrates that Nd-NGQDs experience maximum accumulation 12 h after treatment. The decrease in the fluorescence signal from cells after these time points suggests the excretion of Nd-NGQDs. Confocal fluorescence microscopy of the median plane of cells allows observing Nd-NGQDs that have been internalized inside the cell, disregarding the NGQDs only attached to the membrane (Figure 16 (b)). Bright-field/VIS fluorescence confocal cell image overlays verify the successful internalization and stable VIS fluorescence of Nd-NGQDs inside the cells at 12 h of the optimal imaging time point. Visible fluorescence inside the cells demonstrates that Nd-NGQDs can serve as an intracellular therapeutic tracking agent.

Based on the Nd-NGQDs NIR fluorescence, emission within the cells is recorded with 808 nm laser and 1060 nm emission due to Nd dopant. The fluorescence intensity per area within the cell is used as a measure of internalization/excretion dynamics of Nd-NGQDs in the HEK-293 cells over similar time points: 1, 6, 12, 24, and 48 h. This analysis demonstrates that Nd-NGQDs experience maximum accumulation 12 h after treatment (Figure 17 (a,b)). These results are similar to the internalization/excretion study of Nd-NGQDs in the VIS and indicate that fluorescence from Nd dopant is stable within the intracellular environment, and verify the presence of Nd-NGQDs within the cells. Overall, Nd-NGQDs exhibit fluorescence in the NIR *in vitro* confirming their potential for *in vivo* imaging.

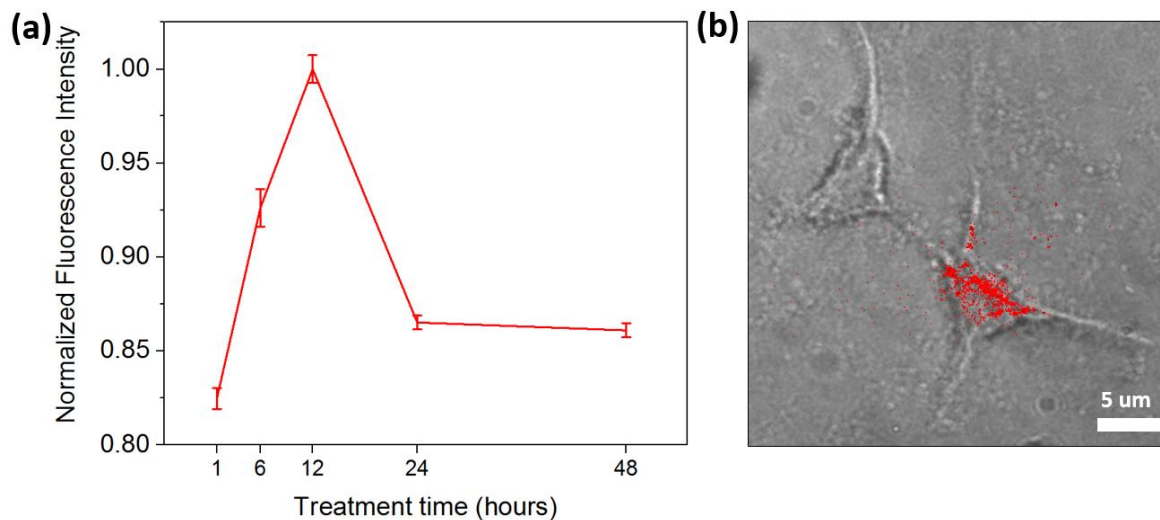


Figure 17. (a) Cellular internalization/excretion dynamics of Nd-NGQDs samples over 1, 6, 12, 24, and 48 h based on the fluorescence intensity of Nd-NGQDs within the HEK-293 cells in the NIR (808 nm excitation, 1060 nm emission). (b) Bright-field/NIR fluorescence overlay images of HEK-293 cells treated with Nd-NGQDs at their optimal internalization time point of 12 hours.

3.6. Internalization of GQD/siRNA complexes

Confocal fluorescence microscopy is utilized in this work to assess the delivery of siEGFR and siKRAS into HeLa cells by the GQDs. Both siEGFR and siKRAS were labeled with ROX and complexed with either NGQDs or Nd-NGQDs to form four combinations: NGQD/siEGFR-ROX, NGQD/siKRAS-ROX, Nd-NGQD/siEGFR-ROX and Nd-NGQD/siKRAS-ROX. These complexes were left to transfect HeLa cells for 12 h, which has been previously determined as an optimal internalization time for both GQD types [65, 132]. In order to separately image fluorescence from GQDs and ROX, those were spectrally separated by exciting at 480 and 540 nm respectively with corresponding emission recorded at 535 ± 20 nm and 600 ± 20 nm (Figure 18). Confocal images taken at a median plane within the cells, demonstrate only fluorescence from the internalized GQDs and siRNA-ROX disregarding those accumulated on the cell membrane.

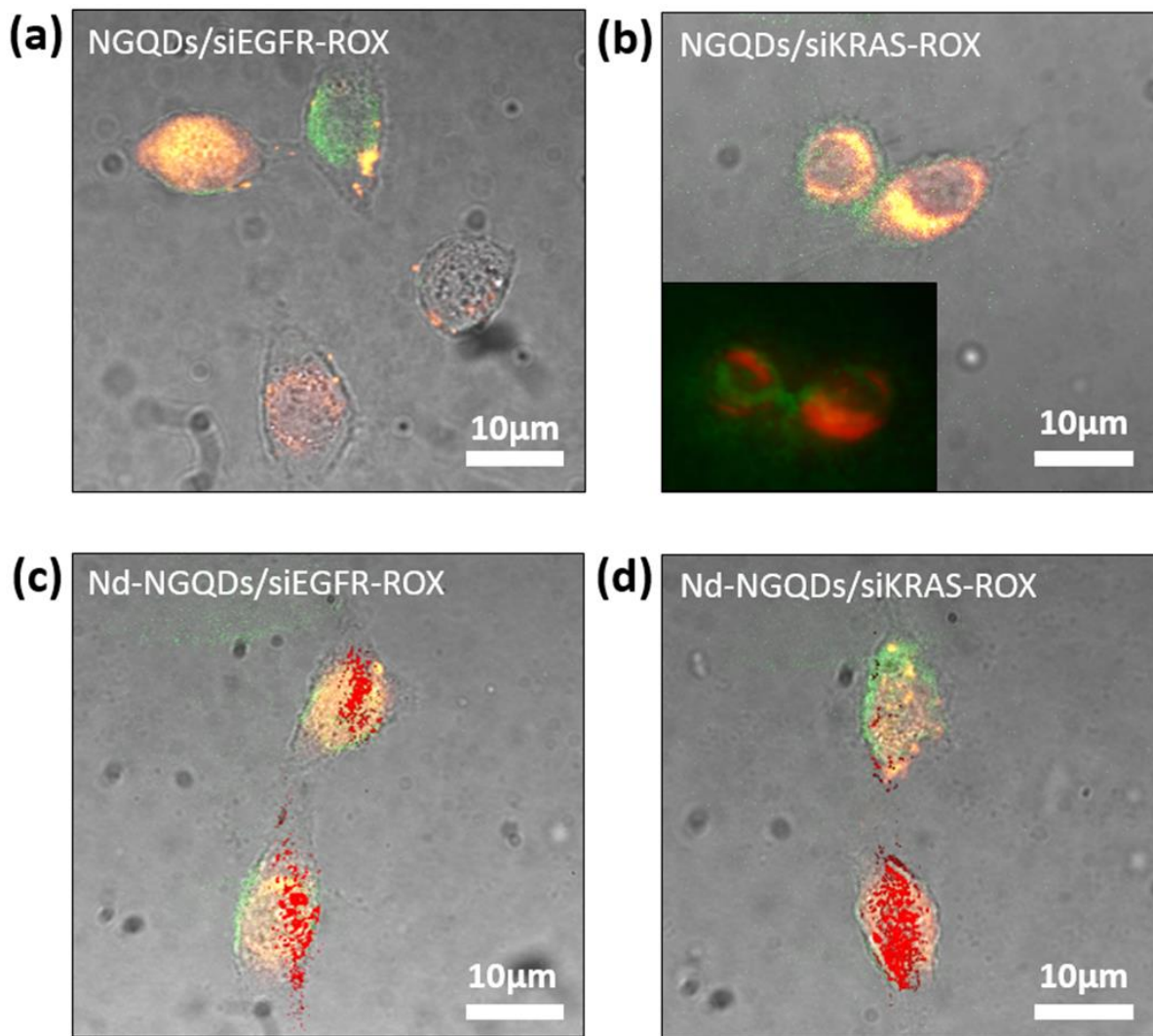


Figure 18. Bright field/visible fluorescence confocal overlay images of HeLa cells treated with (a) NGQD/siEGFR-ROX, (b) NGQD/siKRAS-ROX, (c) NGQD/siEGFR-ROX and (d) Nd-NGQD/siKRAS-ROX for 12 h. GQD (shown in green) is excited with 480 ± 20 nm and collected at 535 ± 20 nm, ROX (shown in orange) is excited with 540 ± 20 nm and collected at 600 ± 20 nm. (c) and (d) also include the overlay of NIR fluorescence arising from internalized Nd-NGQDs. Nd-NGQD (shown in red) is excited with 808 nm laser and collected in the range of 850-1350 nm. (b) Inset: 3D confocal image of green GQD and orange ROX fluorescence in the HeLa cell treated with NGQD/siKRAS-ROX.

Considering substantial GQD fluorescence and ROX emission observed within the cells (Figure 18), we infer that these complexes successfully transfected the cells. This is further confirmed by reconstructing a 3D image of fluorescence within the cells (Figure 18 (b), inset) from individual imaging planes by z-stacking. A resulting orange and green fluorescence

filling the cell demonstrates the presence of both NGQDs and siKRAS-ROX within HeLa cells. As anticipated, NGQDs and Nd-NGQDs are mostly localized in the cytoplasm of HeLa cells [140], while siEGFR and siKRAS are also present in the cytoplasm and can be found translocated into the nucleus [141]. NIR emission from Nd-NGQDs within the HeLa cells collected via hyperspectral microscopy with 808 nm excitation, further confirms their successful internalization and potential for NIR imaging applications *in vivo*. These results verify the successful transfection of GQD/siRNA complexes into HeLa cells, however, do not provide proof of their therapeutic efficacy.

Does the GQD/siRNA complexes lead to cancer gene silencing?

3.7. Protein knockdown by GQD/siRNA complexes

In order to evaluate the gene silencing ability of GQD/siRNA complexes, the levels of the corresponding protein expression were assessed via western blot analysis. NGQDs and Nd-NGQDs at biocompatible 375 $\mu\text{g/mL}$ concentrations were set to transfect HeLa cells for 48 hours to ensure that the platforms themselves do not dysregulate the expression of EGFR and KRAS proteins. At that point, no change in protein expression with respect to the untreated blank control group (Figure 19) was observed suggesting that the therapeutic contribution of the GQDs is negligible.

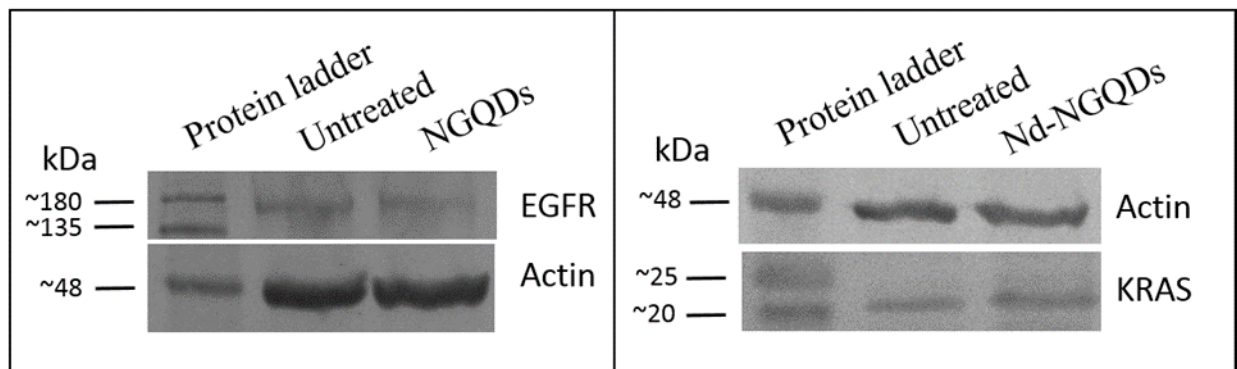


Figure 19. Western blots of NGQDs and Nd-NGQDs at 375 $\mu\text{g/mL}$ concentrations.

Exposing HeLa cells to NGQD/siEGFR, Nd-NGQD/siEGFR, NGQD/siKRAS, or Nd-NGQD/siKRAS complexes at different weight ratios but at a constant 375 $\mu\text{g/mL}$ GQD concentration shows a pattern of protein inhibition for all four complexes (Figure 20). Lipofectamine 3000 known to facilitate successful siRNA transfection is used as a positive control delivering 0.25 nmol/mL of each siRNA. Actin is utilized as a protein expression control, as it is expressed within all eukaryotic cell types and is usually not affected by cellular treatments [142]. As a result, NGQD/siEGFR and Nd-NGQD/siEGFR complexes facilitate the

reduction of the EGFR expression level down to $31.3\pm 8.0\%$ and $36.0\pm 7.5\%$ at the 1:0.1 and 1:0.01 GQD/siRNA weight ratios (Figure 20 (a)). A less effective protein knockdown at higher siRNA ratios can be explained by the specifics of GQD/siRNA complexation: larger amounts of siRNA might both generate a highly negative charge on the complex hampering its internalization and hinder the release of the neighboring siRNA sequences from the GQD surface. Furthermore, using high concentrations of siRNA could lead to off-target effects [143]. Similarly to EGFR knockdown, the expression of KRAS protein is also inhibited by NGQD/siKRAS and Nd-NGQD/siKRAS complexes with nearly maximum inhibition down to 51.5 ± 12.0 and $45.3\pm 14.4\%$ observed at 1:0.01 GQD/siRNA weight ratio (Figure 20 (b)). This inhibition is comparable to the effect of the Lipofectamine positive control. It is noteworthy that KRAS knockdown does not exhibit substantial dependence on the type of platform or the weight ratio between GQDs and siRNA. Given the successful inhibition of KRAS and EGFR at nanomolar gene concentrations down to 31-36% and 45-51%, respectively, GQD/siRNA complexes can be further utilized as new promising therapeutic tools in cancer treatment.

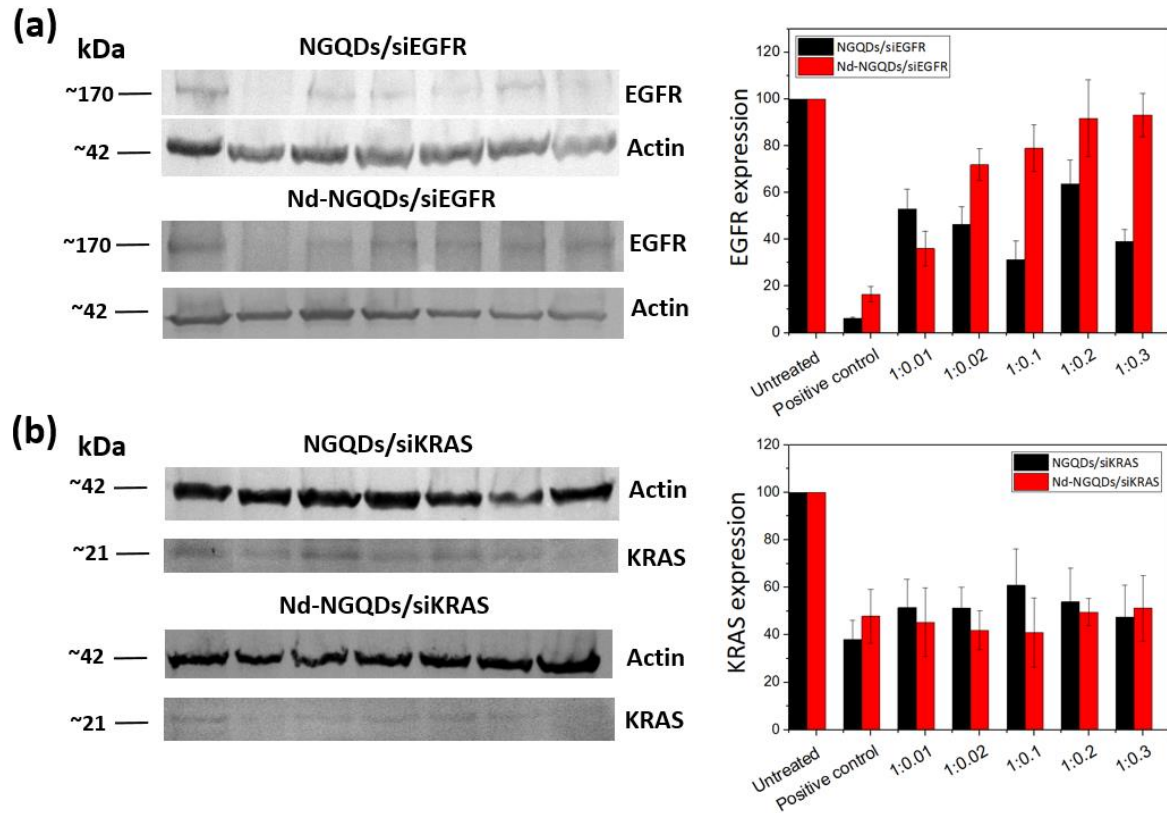


Figure 20. Representative Western blot images and quantification of the blots upon the treatment of HeLa cells with (a) NGQD/siEGFR and Nd-NGQD/siEGFR, (b) NGQD/siKRAS and Nd-NGQD/siKRAS complexes at different GQD/siRNA weight ratios. Lipofectamine 3000 is used as a positive control. EGFR and KRAS protein expression is normalized by actin protein loading and presented as percentage of the untreated sample. Values represent the mean \pm SE of three independent experiments.

4. Conclusion

4.1. Conclusion

In this work, highly biocompatible near-infrared-emissive graphene quantum dots are utilized for the first time as nanocarriers for RNA interference therapy. Nitrogen-doped NGQDs as well as nitrogen and neodymium-doped Nd-NGQDs are synthesized via a cost-effective and scalable hydrothermal microwave-assisted approach with a single glucosamine carbon precursor. Resulting few nanometers in size GQD structures exhibit intrinsic visible fluorescence, as well as fluorescence in the NIR arising from the neodymium dopants. Both NGQDs and Nd-NGQDs form complexes with siEGFR and siKRAS as confirmed by zeta potential and gel retardation assay, with electrostatically most efficient complexation at 1:0.01 GQD/siRNA weight ratio. Theoretical geometry optimization calculation reveals plausible GQD/siRNA complex structures that possess the potential for electrostatic interaction. TEM and HRTEM images confirm the presence of larger structures that can represent modeled complexes. NGQD/siEGFR, Nd-NGQD/siEGFR, NGQD/siKRAS, and Nd-NGQD/siKRAS hybrids at 1:0.01 weight ratio demonstrate high biocompatibility at 375 $\mu\text{g/mL}$ GQD concentration and successful internalization into HeLa cells confirmed by confocal fluorescence microscopy accumulating mostly in the cytoplasm. Within the cells, GQD/siRNA complexes facilitate substantial inhibition of EGFR and KRAS protein expression down to 31-45 %, which for Nd-NGQD/KRAS delivery can surpass the knockdown levels achieved with Lipofectamine 3000. Unlike Lipofectamine 3000, Nd-NGQDs can also perform NIR fluorescence imaging in HeLa cells with 808 nm laser excitation, showing their potential for *in vivo* gene delivery with NIR image tracking. Overall, both NGQDs and Nd-NGQDs are

demonstrated here as successful nanocarriers facilitating image-guided *in vitro* anticancer siRNA delivery with corresponding gene knockdown.

4.2. Questions answered

- i. Are GQDs suitable for siRNA delivery with imaging capabilities?

Both NGQDs and Nd-NGQDs are suitable for siRNA delivery with imaging capabilities. The size of GQDs does not exceed 4 nm allowing for effective cellular internalization. Hydroxyl and carboxyl groups enable high water solubility of GQDs, while amino groups present on the surface of the GQDs provide positive charge and the ability to be complexed with nucleic acids. The gel retardation assay of GQDs and siRNA mixed at different weight ratios demonstrates the best complexation at 100:1 weight ratio (GQDs:siRNA) for both types of GQDs loaded with siKRAS and siEGFR. GQD/siRNA complexes demonstrate ~70-80% cell viability at 375 ug/mL concentration of GQDs. Both GQD types exhibit fluorescence in the visible and provide an essential *in vitro* imaging modality enabling tracing the internalization of the GQDs into biological cells. NGQDs are successfully doped with Nd (~1 atomic %) forming Nd-NGQDs that demonstrate fluorescence emission peak at 1060 nm in the NIR making them a prospective tool for *in vivo* applications. Thus given successful complexation with the siRNA verified via gel retardation assays as well as retention by the GQDs of their visible and NIR imaging capabilities, we can consider that GQDs are suitable for siRNA delivery and possess imaging capabilities.

- ii. Can GQD/siRNA complexes transfect HeLa cells and be used for imaging *in vitro*?

NGQD/siRNA and Nd-NGQD/siRNA can both be imaged in the visible, while Nd-NGQD/siRNA can be also imaged in the near-infrared due to the Nd dopant.

Internalization/excretion studies in the visible and NIR demonstrate that Nd-NGQDs experience maximum accumulation within cells 12 h after treatment. *In vitro* imaging studies show that GQDs and siRNA tagged with ROX dye are successfully transfected HeLa cells after 12 h treatment and mostly accumulate in the cytoplasm. Confocal images verify that visible GQD fluorescence originates from within the cells. As a result, we infer that NGQDs and Nd-NGQDs can be used for image-guided delivery with tracking capabilities in the visible and also in the near infrared, suggesting their further potential for *in vivo* siRNA delivery tracking.

iii. Does the GQD/siRNA complexes lead to cancer gene silencing?

Western blot assay results show that the GQD/siRNA complex facilitates gene silencing and corresponding EGFR and KRAS protein knockdown. Within the HeLa cells GQD/siRNA complexes produce substantial inhibition of EGFR and KRAS protein expression down to 31-45 %, which for GQD/KRAS delivery can surpass the knockdown levels achieved with commercial Lipofectamine 3000. Overall, NGQDs and Nd-NGQDs are found to be promising platforms for siRNA delivery in RNAi therapeutics.

4.3. Future Studies

Our next step will be detailed studies of cellular uptake mechanisms of GQDs by cancerous and non-cancerous cells. We will study the effect of the charge of the GQDs prepared from different precursors on overall uptake and different endocytosis pathways such as micropinocytosis, clathrin-mediated endocytosis or receptor-mediated endocytosis, and caveolin-mediated endocytosis [139]. This step will elucidate the cell internalization pathways and improve the design of the multifunctional GQDs for gene delivery in the future. In case of

the strong charge dependence on overall uptake and endocytosis paths, we will utilize GQDs that demonstrate the highest uptake in cancerous cells for successful siRNA delivery with higher gene transfection efficiency.

We will also perform quantitative polymerase chain reaction (qPCR) analysis in order to confirm mRNA reduction following siRNA administration in HeLa cells [74]. This experiment will demonstrate whether protein-level silencing is accomplished via transcriptional or post-transcriptional gene silencing. The results will be compared with western blot analysis of EGFR and KRAS protein expression.

Prior to further animal work, we will test a novel strategy in cancer treatment as combination therapy. siRNA therapy will be combined with a chemotherapy agent, for example, cisplatin, in overcoming multidrug resistance, reducing off-target toxicity, and achieving potential synergistic apoptotic effects in cancer cells [144]. It was already shown that targeted silencing of both VEGFR2 and EGFR expression by siRNA, combined with low-dose cisplatin, effectively inhibits tumor growth [145]. We will aim to improve on that result and facilitate image-tracking with GQD delivery.

Our last step will be testing the GQD/siRNA complex *in vivo*. We will first conduct a toxicity study to define the minimum concentration of GQD/siRNA complex to use in non-small cell lung cancer (NSCLC) A549 tumor xenograft mouse models. The NIR fluorescence properties of Nd-NGQDs were already shown *in vivo* where GQDs demonstrated successful emission at 1060 nm at the concentration of 0.25 mg/mL [121]. After periodical treatment with GQD/siRNA complex, we expect to observe substantial tumor volume reduction. qPCR and western blot analysis will be performed *ex vivo* to evaluate protein expression inhibition.

GQD/siRNA complex will also be combined with a chemotherapy agent in the case of successful results *in vitro*.

References

1. Zhao, C., et al., *Synthesis of graphene quantum dots and their applications in drug delivery*. Journal of Nanobiotechnology, 2020. **18**(1): p. 1-32.
2. Biswas, M.C., et al., *Graphene Quantum Dots (GQDs) for Bioimaging and Drug Delivery Applications: A Review*. ACS Materials Letters, 2021. **3**(6): p. 889-911.
3. Perini, G., et al., *Unravelling the potential of graphene quantum dots in biomedicine and neuroscience*. International journal of molecular sciences, 2020. **21**(10): p. 3712.
4. Hai, X., et al., *Tuning the optical properties of graphene quantum dots for biosensing and bioimaging*. Journal of Materials Chemistry B, 2018. **6**(20): p. 3219-3234.
5. Kansara, V., et al., *Graphene quantum dots: synthesis, optical properties and navigational applications against cancer*. Materials Today Communications, 2022: p. 103359.
6. Li, G., et al., *A ratiometric fluorescent composite nanomaterial for RNA detection based on graphene quantum dots and molecular probes*. Journal of Materials Chemistry B, 2018. **6**(26): p. 4380-4384.
7. Landry, M.P., *Graphene Quantum Dot oxidation Governs noncovalent Biopolymer Adsorption*.
8. Ajgaonkar, R., et al., *Detection of pancreatic cancer miRNA with biocompatible nitrogen-doped graphene quantum dots*. Materials, 2022. **15**(16): p. 5760.
9. Wu, C., et al., *Ultrasensitive detection of protein based on graphene quantum dots with resonance light scattering technique*. Journal of Nanoscience and Nanotechnology, 2018. **18**(4): p. 2680-2685.
10. Xu, A., et al., *Selective supramolecular interaction of ethylenediamine functionalized graphene quantum dots: Ultra-sensitive photoluminescence detection for nickel ion in vitro*. Synthetic Metals, 2018. **244**: p. 106-112.
11. Chung, S., R.A. Revia, and M. Zhang, *Graphene quantum dots and their applications in bioimaging, biosensing, and therapy*. Advanced Materials, 2021. **33**(22): p. 1904362.
12. Alberts, B., et al., *Essential cell biology: Fifth international student edition*. 2018: WW Norton & Company.
13. Shimamoto, Y., S. Redemann, and D. Needleman, *Mechanics of Cell Division*. 2020, Frontiers Media SA. p. 620111.
14. Laugesen, M., et al., *Hand-rolled cigarette smoking patterns compared with factory-made cigarette smoking in New Zealand men*. BMC Public Health, 2009. **9**(1): p. 1-6.
15. D'Orazio, J., et al., *UV radiation and the skin*. International journal of molecular sciences, 2013. **14**(6): p. 12222-12248.
16. Bansal, A., M.P. Singh, and B. Rai, *Human papillomavirus-associated cancers: A growing global problem*. International Journal of Applied and Basic Medical Research, 2016. **6**(2): p. 84.
17. Pfeffer, C.M. and A.T. Singh, *Apoptosis: a target for anticancer therapy*. International journal of molecular sciences, 2018. **19**(2): p. 448.
18. Arruebo, M., et al., *Assessment of the evolution of cancer treatment therapies*. Cancers, 2011. **3**(3): p. 3279-3330.
19. Abbas, Z. and S. Rehman, *An overview of cancer treatment modalities*. Neoplasms, 2018. **1**: p. 139-157.
20. Moses, M.A., H. Brem, and R. Langer, *Advancing the field of drug delivery: taking aim at cancer*. Cancer cell, 2003. **4**(5): p. 337-341.
21. El-Readi, M.Z. and M.A. Althubiti, *Cancer nanomedicine: a new era of successful targeted therapy*. Journal of Nanomaterials, 2019. **2019**: p. 1-13.

22. Debela, D.T., et al., *New approaches and procedures for cancer treatment: Current perspectives*. SAGE open medicine, 2021. **9**: p. 20503121211034366.
23. Fairchild, A., et al., *Hormonal therapy in oncology: a primer for the radiologist*. American Journal of Roentgenology, 2015. **204**(6): p. W620-W630.
24. Arabi, F., V. Mansouri, and N. Ahmadbeigi, *Gene therapy clinical trials, where do we go? An overview*. Biomedicine & Pharmacotherapy, 2022. **153**: p. 113324.
25. Hollingsworth, R.E. and K. Jansen, *Turning the corner on therapeutic cancer vaccines*. npj Vaccines, 2019. **4**(1): p. 7.
26. Ventola, C.L., *Cancer immunotherapy, part 1: current strategies and agents*. Pharmacy and therapeutics, 2017. **42**(6): p. 375.
27. Ventola, C.L., *Cancer immunotherapy, part 2: efficacy, safety, and other clinical considerations*. Pharmacy and Therapeutics, 2017. **42**(7): p. 452.
28. Charbe, N.B., et al., *Small interfering RNA for cancer treatment: overcoming hurdles in delivery*. Acta Pharmaceutica Sinica B, 2020. **10**(11): p. 2075-2109.
29. Zhang, H., et al., *Application of the CRISPR/Cas9-based gene editing technique in basic research, diagnosis, and therapy of cancer*. Molecular Cancer, 2021. **20**: p. 1-22.
30. Seow, Y. and M.J. Wood, *Biological gene delivery vehicles: beyond viral vectors*. Molecular therapy, 2009. **17**(5): p. 767-777.
31. Xu, H., Z. Li, and J. Si, *Nanocarriers in gene therapy: a review*. Journal of biomedical nanotechnology, 2014. **10**(12): p. 3483-3507.
32. Li, X.-J., et al., *Gene delivery in peritoneal dialysis related peritoneal fibrosis research*. Chinese Medical Journal, 2012. **125**(12): p. 2219-2224.
33. Unzu, C., et al., *Innate functions of immunoglobulin M lessen liver gene transfer with helper-dependent adenovirus*. PLoS One, 2014. **9**(1): p. e85432.
34. Wang, B., et al., *Regression of atherosclerosis plaques in apolipoprotein E^{-/-} mice after lentivirus-mediated RNA interference of CD40*. International journal of cardiology, 2013. **163**(1): p. 34-39.
35. Gmeiner, W.H. and S. Ghosh, *Nanotechnology for cancer treatment*. Nanotechnology reviews, 2014. **3**(2): p. 111-122.
36. Hapuarachchige, S. and D. Artemov, *Theranostic pretargeting drug delivery and imaging platforms in cancer precision medicine*. Frontiers in oncology, 2020. **10**: p. 1131.
37. Islam, M.A., et al., *Regulation of endocytosis by non-viral vectors for efficient gene activity*. Journal of biomedical nanotechnology, 2014. **10**(1): p. 67-80.
38. Khafaji, M., et al., *Inorganic nanomaterials for chemo/photothermal therapy: a promising horizon on effective cancer treatment*. Biophysical reviews, 2019. **11**: p. 335-352.
39. Yang, F., et al., *Nanoparticle-based drug delivery systems for the treatment of cardiovascular diseases*. Bioactive Substances-Mediated Targeted Therapy of Cardio-Cerebrovascular Diseases, 2023. **16648714**: p. 95.
40. He, S., et al., *Metal-organic frameworks for advanced drug delivery*. Acta Pharmaceutica Sinica B, 2021. **11**(8): p. 2362-2395.
41. Gryczynski, Z.K. and I. Gryczynski, *Practical fluorescence spectroscopy*. 2019: CRC Press.
42. Würth, C., et al., *Relative and absolute determination of fluorescence quantum yields of transparent samples*. Nature protocols, 2013. **8**(8): p. 1535-1550.
43. Demchenko, A.P., *Photobleaching of organic fluorophores: quantitative characterization, mechanisms, protection*. Methods and applications in fluorescence, 2020. **8**(2): p. 022001.
44. Cornea, A. and P.M. Conn, *Fluorescence microscopy: Super-resolution and other novel techniques*. 2014.
45. Liang, W., A.J. Mason, and J.K. Lam, *Western blot evaluation of siRNA delivery by pH-responsive peptides*. Target Identification and Validation in Drug Discovery: Methods and Protocols, 2013: p. 73-87.

46. Xu, X., et al., *Electrophoretic analysis and purification of fluorescent single-walled carbon nanotube fragments*. Journal of the American Chemical Society, 2004. **126**(40): p. 12736-12737.
47. Ghosh, D., et al., *Current and future perspectives of carbon and graphene quantum dots: From synthesis to strategy for building optoelectronic and energy devices*. Renewable and Sustainable Energy Reviews, 2021. **135**: p. 110391.
48. Sun, Y.-P., et al., *Quantum-sized carbon dots for bright and colorful photoluminescence*. Journal of the American Chemical Society, 2006. **128**(24): p. 7756-7757.
49. Ye, R., et al., *Coal as an abundant source of graphene quantum dots*. Nature communications, 2013. **4**(1): p. 2943.
50. Peng, J., et al., *Graphene quantum dots derived from carbon fibers*. Nano letters, 2012. **12**(2): p. 844-849.
51. Zhu, H., et al., *Microwave synthesis of fluorescent carbon nanoparticles with electrochemiluminescence properties*. Chemical Communications, 2009(34): p. 5118-5120.
52. Zhai, X., et al., *Highly luminescent carbon nanodots by microwave-assisted pyrolysis*. Chemical communications, 2012. **48**(64): p. 7955-7957.
53. Zhang, B., C.y. Liu, and Y. Liu, *A novel one-step approach to synthesize fluorescent carbon nanoparticles*. 2010, Wiley Online Library.
54. Yang, Z.-C., et al., *Intrinsically fluorescent carbon dots with tunable emission derived from hydrothermal treatment of glucose in the presence of monopotassium phosphate*. Chemical communications, 2011. **47**(42): p. 11615-11617.
55. Bourlinos, A.B., et al., *Surface functionalized carbogenic quantum dots*. small, 2008. **4**(4): p. 455-458.
56. Younis, M.R., et al., *Recent advances on graphene quantum dots for bioimaging applications*. Frontiers in Chemistry, 2020. **8**: p. 424.
57. Frieler, M., et al., *Effects of doxorubicin delivery by nitrogen-doped graphene quantum dots on cancer cell growth: experimental study and mathematical modeling*. Nanomaterials, 2021. **11**(1): p. 140.
58. Liang, J., et al., *Versatile nanoplatform loaded with doxorubicin and graphene quantum dots/methylene blue for drug delivery and chemophotothermal/photodynamic synergetic cancer therapy*. ACS Applied Bio Materials, 2020. **3**(10): p. 7122-7132.
59. Ghafary, S.M., et al., *Simultaneous gene delivery and tracking through preparation of photoluminescent nanoparticles based on graphene quantum dots and chimeric peptides*. Scientific reports, 2017. **7**(1): p. 1-14.
60. Li, L.-s. and X. Yan, *Colloidal graphene quantum dots*. The Journal of Physical Chemistry Letters, 2010. **1**(17): p. 2572-2576.
61. Wang, S., et al., *The dual roles of functional groups in the photoluminescence of graphene quantum dots*. Nanoscale, 2016. **8**(14): p. 7449-7458.
62. Chien, C.T., et al., *Tunable photoluminescence from graphene oxide*. Angewandte Chemie International Edition, 2012. **51**(27): p. 6662-6666.
63. Wang, L., et al., *Direct Observation of Quantum-Confined Graphene-Like States and Novel Hybrid States in Graphene Oxide by Transient Spectroscopy*. Advanced materials, 2013. **25**(45): p. 6539-6545.
64. Yeh, T.-F., et al., *Elucidating quantum confinement in graphene oxide dots based on excitation-wavelength-independent photoluminescence*. The journal of physical chemistry letters, 2016. **7**(11): p. 2087-2092.
65. Campbell, E., et al., *Doped graphene quantum dots for intracellular multicolor imaging and cancer detection*. ACS Biomaterials Science & Engineering, 2019. **5**(9): p. 4671-4682.
66. Khan, W.U., D. Wang, and Y. Wang, *Highly green emissive nitrogen-doped carbon dots with excellent thermal stability for bioimaging and solid-state LED*. Inorganic chemistry, 2018. **57**(24): p. 15229-15239.

67. Röding, M., et al., *Fluorescence lifetime analysis of graphene quantum dots*. The Journal of Physical Chemistry C, 2014. **118**(51): p. 30282-30290.
68. Franco, Z., et al. *Nanosecond fluorescence lifetime low-cost sensor*. in *SENSORS, 2014 IEEE*. 2014. IEEE.
69. Berezin, M.Y. and S. Achilefu, *Fluorescence lifetime measurements and biological imaging*. Chemical reviews, 2010. **110**(5): p. 2641-2684.
70. Hasan, M.T., et al., *Photo-and electroluminescence from nitrogen-doped and nitrogen-sulfur codoped graphene quantum dots*. Advanced Functional Materials, 2018. **28**(42): p. 1804337.
71. Jeong, S., et al., *Graphene quantum dot oxidation governs noncovalent biopolymer adsorption*. Scientific reports, 2020. **10**(1): p. 7074.
72. Wang, J., et al., *High efficient delivery of siRNA into tumor cells by positively charged carbon dots*. Journal of Macromolecular Science, Part A, 2018. **55**(11-12): p. 770-774.
73. Zhao, X., et al., *Inhibitory effect of aptamer-carbon dot nanomaterial-siRNA complex on the metastasis of hepatocellular carcinoma cells by interfering with FMRP*. European Journal of Pharmaceutics and Biopharmaceutics, 2022. **174**: p. 47-55.
74. Wang, Q., et al., *Fluorescent carbon dots as an efficient siRNA nanocarrier for its interference therapy in gastric cancer cells*. Journal of nanobiotechnology, 2014. **12**(1): p. 1-12.
75. Li, R., et al., *PEI modified orange emissive carbon dots with excitation-independent fluorescence emission for cellular imaging and siRNA delivery*. Carbon, 2021. **177**: p. 403-411.
76. Kim, S., et al., *Highly efficient gene silencing and bioimaging based on fluorescent carbon dots in vitro and in vivo*. Nano Research, 2017. **10**(2): p. 503-519.
77. Siegel, R.L., et al., *Cancer statistics, 2021*. Ca Cancer J Clin, 2021. **71**(1): p. 7-33.
78. Dalmartello, M., et al., *European cancer mortality predictions for the year 2022 with focus on ovarian cancer*. Annals of Oncology, 2022. **33**(3): p. 330-339.
79. Takeshima, H. and T. Ushijima, *Accumulation of genetic and epigenetic alterations in normal cells and cancer risk*. NPJ precision oncology, 2019. **3**(1): p. 1-8.
80. Song, P., et al., *The regulation of protein translation and its implications for cancer*. Signal Transduction and Targeted Therapy, 2021. **6**(1): p. 1-9.
81. Timar, J. and K. Kashofer, *Molecular epidemiology and diagnostics of KRAS mutations in human cancer*. Cancer and Metastasis Reviews, 2020. **39**(4): p. 1029-1038.
82. Pinheiro, G., et al., *Identifying relationships between imaging phenotypes and lung cancer-related mutation status: EGFR and KRAS*. Scientific reports, 2020. **10**(1): p. 1-9.
83. Sigismund, S., D. Avanzato, and L. Lanzetti, *Emerging functions of the EGFR in cancer*. Molecular oncology, 2018. **12**(1): p. 3-20.
84. Hamarsheh, S., et al., *Immune modulatory effects of oncogenic KRAS in cancer*. Nature communications, 2020. **11**(1): p. 1-11.
85. Plattner, C. and H. Hackl, *Modeling therapy resistance via the EGFR signaling pathway*. The FEBS Journal, 2019. **286**(7): p. 1284-1286.
86. Leonetti, A., et al., *Resistance mechanisms to osimertinib in EGFR-mutated non-small cell lung cancer*. British journal of cancer, 2019. **121**(9): p. 725-737.
87. Yuan, X.H., et al., *Association between EGFR/KRAS mutation and expression of VEGFA, VEGFR and VEGFR2 in lung adenocarcinoma*. Oncology letters, 2018. **16**(2): p. 2105-2112.
88. Xu, W., X. Jiang, and L. Huang, *RNA interference technology*. Comprehensive Biotechnology, 2019: p. 560.
89. Ho, V.W.T., et al., *Cancer Management by Tyrosine Kinase Inhibitors: Efficacy, Limitation, and Future Strategies*, in *Tyrosine Kinases as Druggable Targets in Cancer*. 2019, IntechOpen.
90. Dana, H., et al., *Molecular mechanisms and biological functions of siRNA*. International journal of biomedical science: IJBS, 2017. **13**(2): p. 48.
91. Tian, Z., et al., *Insight into the prospects for RNAi therapy of cancer*. Frontiers in Pharmacology, 2021. **12**: p. 644718.

92. Padda, I.S., A.U. Mahtani, and M. Parmar, *Small Interfering RNA (siRNA) Based Therapy*, in *StatPearls [Internet]*. 2022, StatPearls Publishing.
93. Kim, B., J.H. Park, and M.J. Sailor, *Rekindling RNAi therapy: materials design requirements for in vivo siRNA delivery*. *Advanced materials*, 2019. **31**(49): p. 1903637.
94. Paunovska, K., D. Loughrey, and J.E. Dahlman, *Drug delivery systems for RNA therapeutics*. *Nature Reviews Genetics*, 2022. **23**(5): p. 265-280.
95. Shirley, J.L., et al., *Immune responses to viral gene therapy vectors*. *Molecular Therapy*, 2020. **28**(3): p. 709-722.
96. Yan, Y., et al., *Non-viral vectors for RNA delivery*. *Journal of Controlled Release*, 2022.
97. Thi, T.T.H., et al., *Lipid-based nanoparticles in the clinic and clinical trials: from cancer nanomedicine to COVID-19 vaccines*. *Vaccines*, 2021. **9**(4): p. 359.
98. Torres-Vanegas, J.D., J.C. Cruz, and L.H. Reyes, *Delivery systems for nucleic acids and proteins: Barriers, cell capture pathways and nanocarriers*. *Pharmaceutics*, 2021. **13**(3): p. 428.
99. Gao, H., R. Cheng, and H. A. Santos, *Nanoparticle-mediated siRNA delivery systems for cancer therapy*. *View*, 2021. **2**(3): p. 20200111.
100. Li, D., et al., *Nanoparticles as drug delivery systems of RNAi in cancer therapy*. *Molecules*, 2021. **26**(8): p. 2380.
101. Artiga, Á., et al., *Current status and future perspectives of gold nanoparticle vectors for siRNA delivery*. *Journal of Materials Chemistry B*, 2019. **7**(6): p. 876-896.
102. Kong, L., et al., *Multifunctional PEI-entrapped gold nanoparticles enable efficient delivery of therapeutic siRNA into glioblastoma cells*. *Biomaterials science*, 2017. **5**(2): p. 258-266.
103. Rahme, K., J. Guo, and J.D. Holmes, *Bioconjugated gold nanoparticles enhance siRNA delivery in prostate cancer cells*, in *Rna interference and cancer therapy*. 2019, Springer. p. 291-301.
104. Schwarz, B. and O.M. Merkel, *Functionalized PEI and its role in gene therapy*. *Mater Matters*, 2017. **12**: p. 2.
105. Zare, H., et al., *Carbon nanotubes: Smart drug/gene delivery carriers*. *International journal of nanomedicine*, 2021. **16**: p. 1681.
106. Amenta, V. and K. Aschberger, *Carbon nanotubes: potential medical applications and safety concerns*. *Wiley Interdisciplinary Reviews: Nanomedicine and Nanobiotechnology*, 2015. **7**(3): p. 371-386.
107. NiBler, R., et al., *Sensing with chirality-pure near-infrared fluorescent carbon nanotubes*. *Analytical Chemistry*, 2021. **93**(16): p. 6446-6455.
108. Wang, T., et al., *Recent Progress in Second Near-Infrared (NIR-II) Fluorescence Imaging in Cancer*. *Biomolecules*, 2022. **12**(8): p. 1044.
109. Kirkpatrick, D.L., et al., *Carbon nanotubes: solution for the therapeutic delivery of siRNA?* *Materials*, 2012. **5**(2): p. 278-301.
110. Demirer, G.S., et al., *Carbon nanocarriers deliver siRNA to intact plant cells for efficient gene knockdown*. *Science advances*, 2020. **6**(26): p. eaaz0495.
111. Campbell, E., et al., *Graphene oxide as a multifunctional platform for intracellular delivery, imaging, and cancer sensing*. *Scientific reports*, 2019. **9**(1): p. 1-9.
112. Wang, Y., et al., *Functionalized folate-modified graphene oxide/PEI siRNA nanocomplexes for targeted ovarian cancer gene therapy*. *Nanoscale research letters*, 2020. **15**(1): p. 1-11.
113. Chen, S., et al., *Anti-EpCAM functionalized graphene oxide vector for tumor targeted siRNA delivery and cancer therapy*. *Asian journal of pharmaceutical sciences*, 2021. **16**(5): p. 598-611.
114. Murjani, B.O., et al., *Carbon nanotubes in biomedical applications: current status, promises, and challenges*. *Carbon Letters*, 2022: p. 1-20.
115. Ghulam, A.N., et al., *Graphene Oxide (GO) Materials—Applications and Toxicity on Living Organisms and Environment*. *Journal of Functional Biomaterials*, 2022. **13**(2): p. 77.

116. Smith, A.M., M.C. Mancini, and S. Nie, *Second window for in vivo imaging*. Nature nanotechnology, 2009. **4**(11): p. 710-711.
117. Hasan, M.T., et al., *Near-infrared emitting graphene quantum dots synthesized from reduced graphene oxide for in vitro/in vivo/ex vivo bioimaging applications*. 2D Materials, 2021. **8**(3): p. 035013.
118. Wei, X., et al., *Photoluminescence quantum yield of single-wall carbon nanotubes corrected for the photon reabsorption effect*. Nano Letters, 2019. **20**(1): p. 410-417.
119. Genovese, D., et al., *Tandem dye-doped nanoparticles for NIR imaging via cerenkov resonance energy transfer*. Frontiers in Chemistry, 2020. **8**: p. 71.
120. Franke, D., et al., *Continuous injection synthesis of indium arsenide quantum dots emissive in the short-wavelength infrared*. Nature communications, 2016. **7**(1): p. 12749.
121. Hasan, M.T., et al., *Rare-earth metal ions doped graphene quantum dots for near-ir in vitro/in vivo/ex vivo imaging applications*. Advanced Optical Materials, 2020. **8**(21): p. 2000897.
122. Ning, Y., M. Zhu, and J.-L. Zhang, *Near-infrared (NIR) lanthanide molecular probes for bioimaging and biosensing*. Coordination Chemistry Reviews, 2019. **399**: p. 213028.
123. Eichhorn, M., *Quasi-three-level solid-state lasers in the near and mid infrared based on trivalent rare earth ions*. Applied Physics B, 2008. **93**: p. 269-316.
124. Wang, R. and F. Zhang, *Lanthanide-based near infrared nanomaterials for bioimaging*. 2016.
125. Chen, G., et al., *Core/shell NaGdF₄: Nd³⁺/NaGdF₄ nanocrystals with efficient near-infrared to near-infrared downconversion photoluminescence for bioimaging applications*. ACS nano, 2012. **6**(4): p. 2969-2977.
126. Kamimura, M., et al., *Near-infrared (1550 nm) in vivo bioimaging based on rare-earth doped ceramic nanophosphors modified with PEG-b-poly (4-vinylbenzylphosphonate)*. Nanoscale, 2011. **3**(9): p. 3705-3713.
127. Yang, Y., et al., *Recent advances in design of lanthanide-containing NIR-II luminescent nanoprobos*. Iscience, 2021. **24**(2): p. 102062.
128. Liao, J., et al., *NIR-II emissive properties of 808 nm-excited lanthanide-doped nanoparticles for multiplexed in vivo imaging*. Journal of Luminescence, 2022. **242**: p. 118597.
129. Hanwell, M.D., et al., *Avogadro: an advanced semantic chemical editor, visualization, and analysis platform*. Journal of cheminformatics, 2012. **4**(1): p. 1-17.
130. Halgren, T.A., *Merck molecular force field. I. Basis, form, scope, parameterization, and performance of MMFF94*. Journal of computational chemistry, 1996. **17**(5-6): p. 490-519.
131. Wang, L., et al., *Gram-scale synthesis of single-crystalline graphene quantum dots with superior optical properties*. Nature communications, 2014. **5**(1): p. 1-9.
132. Valimukhametova, A.R., et al., *Dual-Mode Fluorescence/Ultrasound Imaging with Biocompatible Metal-Doped Graphene Quantum Dots*. ACS Biomaterials Science & Engineering, 2022. **8**(11): p. 4965-4975.
133. Campbell, E., et al., *Graphene quantum dot formulation for cancer imaging and redox-based drug delivery*. Nanomedicine: Nanotechnology, Biology and Medicine, 2021. **37**: p. 102408.
134. Ben Aoun, S., *Nanostructured carbon electrode modified with N-doped graphene quantum dots–chitosan nanocomposite: a sensitive electrochemical dopamine sensor*. Royal Society open science, 2017. **4**(11): p. 171199.
135. Baskoro, F., et al., *Graphene oxide-cation interaction: Inter-layer spacing and zeta potential changes in response to various salt solutions*. Journal of Membrane Science, 2018. **554**: p. 253-263.
136. Aydin, O., et al., *Determination of Optimum Ratio of Cationic Polymers and Small Interfering RNA with Agarose Gel Retardation Assay*, in *Antisense RNA Design, Delivery, and Analysis*. 2022, Humana, New York, NY. p. 117-128.
137. Fröhlich, E., *The role of surface charge in cellular uptake and cytotoxicity of medical nanoparticles*. International journal of nanomedicine, 2012. **7**: p. 5577.

138. Ramana, L.N., L.N. Dinh, and V. Agarwal, *Influence of surface charge of graphene quantum dots on their uptake and clearance in melanoma cells*. *Nanoscale Advances*, 2021. **3**(12): p. 3513-3521.
139. Halder, A., et al., *One-pot green synthesis of biocompatible graphene quantum dots and their cell uptake studies*. *ACS Applied Bio Materials*, 2018. **1**(2): p. 452-461.
140. Yuan, X., et al., *Cellular distribution and cytotoxicity of graphene quantum dots with different functional groups*. *Nanoscale research letters*, 2014. **9**(1): p. 1-9.
141. Berezina, S.Y., et al., *siRNA in human cells selectively localizes to target RNA sites*. *Proceedings of the National Academy of Sciences*, 2006. **103**(20): p. 7682-7687.
142. Mahmood, T. and P.-C. Yang, *Western blot: technique, theory, and trouble shooting*. *North American journal of medical sciences*, 2012. **4**(9): p. 429.
143. Caffrey, D.R., et al., *siRNA off-target effects can be reduced at concentrations that match their individual potency*. *PloS one*, 2011. **6**(7): p. e21503.
144. Kumar, K., et al., *New paradigm in combination therapy of siRNA with chemotherapeutic drugs for effective cancer therapy*. *Current Research in Pharmacology and Drug Discovery*, 2022: p. 100103.
145. Chen, S., et al., *Combination therapy with VEGFR2 and EGFR siRNA enhances the antitumor effect of cisplatin in non-small cell lung cancer xenografts*. *Oncology reports*, 2013. **29**(1): p. 260-268.

VITA

PERSONAL

Alina Valimukhametova
Satpayev, Kazakhstan
November 3, 1995

EDUCATION

Spring 2020-Present

Texas Christian University
Department of Physics & Astronomy
Graduate Student

Fall 2017 - Summer 2019

Kazan Federal University
Department of Solid State Physics
Master of Science, Physics

Fall 2013 - Summer 2017

Kazan Federal University
Department of Solid State Physics
Bachelor of Science, Nanotechnology

PUBLICATIONS

1. **Valimukhametova, A.**; Lee, B.; Topkiran, U.; Gries, K.; Gonzalez-Rodriguez, R.; Coffey, J.; Akkaraju, G.; Naumov, A. Cancer Therapeutic siRNA Delivery and Imaging by Nitrogen and Neodymium-Doped Graphene Quantum Dots, *MDPI Nanomaterials* (Submitted Journal Paper)
2. Lee, B.; Stokes, G.; **Valimukhametova, A.**; Nguyen, S.; Gonzalez-Rodriguez, R.; Bhaloo A.; Coffey, J.; Naumov, A.V. Automated Approach to In Vitro Image-Guided Photothermal Therapy with Top-Down and Bottom-Up-Synthesized Graphene Quantum Dots, *MDPI Nanomaterials*, 2023, 13(5), 805.
3. **Valimukhametova, A.**; Zub, O.; Lee, B.; Fannon O.; Nguyen, S.; Gonzalez-Rodriguez, R.; Akkaraju, G.R.; Naumov, A.V. Dual-Mode Fluorescence/Ultrasonography Imaging with Biocompatible Metal-Doped Graphene Quantum Dots. *ACS Biomaterials Science & Engineering*, 2022, 8, 11, 4965–4975.
4. Ajgaonkar, R.; Lee, B.; **Valimukhametova, A.**; Nguyen, S.; Gonzalez-Rodriguez, R.; Coffey, J.; Akkaraju, G.R.; Naumov, A.V. Detection of Pancreatic Cancer miRNA with Biocompatible Nitrogen-Doped Graphene Quantum Dots. *Materials* 2022, 15, 5760.
5. Khamidullin, T., Galyaltdinov, S., **Valimukhametova, A.**, Kalinina, I., Dimiev, A.M. Simple, cost-efficient and high throughput method for separating single-wall carbon nanotubes with modified cotton. *Carbon*, 2021, 178, pp. 157–163
6. **Valimukhametova, A.**, Ryan, C., Paz, T., Grote, F., Naumov, A.V. Experimental and theoretical inquiry into optical properties of graphene derivatives. *Nanotechnology*, 2021, 32(1), 015709
7. Lee, B.H., **Valimukhametova, A.**, Ryan, C., Grote, F., Naumov, A.V. Electric field quenching of graphene oxide photoluminescence. *Nanotechnology*, 2020, 31(46), 465203
8. Dimiev, A.M., Lounev, I., Khamidullin, T., **Valimukhametova, A.**, Khannanov, A. Polymer Composites Comprising Single-Atomic-Layer Graphenic Conductive Inclusions and Their Unusual Dielectric Properties. *Journal of Physical Chemistry C*, 2020, 124(25), pp. 13715–13725
9. Khannanov, A., Kiiamov, A., **Valimukhametova, A.**, Vagizov, F.G., Dimiev, A.M. Direct growth of oriented nanocrystals of gamma-iron on graphene oxide substrates. Detailed analysis of the factors affecting unexpected formation of the gamma-iron phase. *New Journal of Chemistry*, 2019, 43(33), pp. 12923–12931
10. **Valimukhametova, A.**, Khannanov, A., Kiiamov, A., Vagizov, F.G., Dimiev, A.M. Growth of invar nanoparticles on a graphene oxide support. *CrystEngComm*, 2019, 21(27), pp. 4092–4097
11. Khannanov, A., Kiiamov, A., **Valimukhametova, A.**, Vagizov, F.G., Dimiev, A.M. γ -Iron Phase Stabilized at Room Temperature by Thermally Processed Graphene Oxide. *Journal of the American Chemical Society*, 2018, 140(29), pp. 9051–9055

Abstract

Cancer Therapeutic siRNA Delivery and Imaging by Nitrogen and Neodymium-Doped

Graphene Quantum Dots

By Alina Valimukhametova, 2023

Department of Physics & Astronomy

Texas Christian University

Thesis Advisor: Anton Naumov

While small interfering RNA (siRNA) technology has become a powerful tool that can enable cancer-specific gene therapy, its translation to the clinic is still hampered by several critical factors. These include the inability of cell transfection by the genes alone, poor siRNA stability in blood, and the lack of delivery tracking capabilities. Recently, graphene quantum dots (GQDs) have emerged as a novel platform allowing targeted drug delivery and fluorescence image-tracking in the visible and near-infrared. These capabilities can aid in overcoming primary obstacles to siRNA therapeutics. Here, for the first time, we utilize biocompatible nitrogen and neodymium-doped graphene quantum dots (NGQDs and Nd-NGQDs) for the delivery of Kirsten rat sarcoma virus (KRAS) and epidermal growth factor receptor (EGFR) siRNA effective against a variety of cancer types. The non-covalent loading of siRNA onto GQDs is evaluated and optimized by the electrophoretic mobility shift assay and zeta potential measurements. GQDs as a delivery platform facilitate successful gene transfection into HeLa cells confirmed by confocal fluorescence microscopy at biocompatible GQD concentrations of 375 $\mu\text{g/mL}$. While the NGQD platform provides visible fluorescence tracking, Nd doping enables deeper tissue near-infrared fluorescence imaging suitable for both *in vitro* and *in vivo* applications. The therapeutic efficacy of the GQD/siRNA complex is verified by successful protein knockdown in HeLa cells at nanomolar siEGFR and siKRAS concentrations. A range of GQD/siRNA loading ratios and payloads is tested to ultimately provide substantial inhibition of protein expression down to 31-45% comparable with conventional Lipofectamine-mediated delivery. This demonstrates the promising potential of GQDs for the non-toxic delivery of siRNA and genes in general, complemented by multiwavelength image-tracking.